

# Airborne observations of peroxy radicals during the EMeRGe campaign in Europe

<sup>1+</sup>Midhun George, <sup>1</sup>Maria Dolores Andrés Hernández, <sup>1\*</sup>Vladyslav Nenakhov, <sup>1</sup>Yangzhuoran Liu, <sup>1</sup>John Philip Burrows; <sup>2</sup>Birger Bohn; <sup>3</sup>Eric Förster, <sup>3</sup>Florian Obersteiner, <sup>3</sup>Andreas Zahn; <sup>4</sup>Theresa Harlaß, <sup>4</sup>Helmut Ziereis, <sup>4</sup>Hans Schlager; <sup>5</sup>Benjamin Schreiner, <sup>5</sup>Flora Kluge, <sup>5</sup>Katja Bigge, and <sup>5</sup>Klaus Pfeilsticker

<sup>1</sup> Institute of Environmental Physics, University of Bremen, Germany

<sup>2</sup> Institute of Energy and Climate Research, IEK-8: Troposphere, Forschungszentrum Jülich GmbH, Jülich, Germany

<sup>3</sup> Institute of Meteorology and Climate Research, Karlsruhe Institute of Technology, Karlsruhe, Germany

<sup>4</sup> Deutsches Zentrum für Luft- und Raumfahrt (DLR), Institut für Physik der Atmosphäre, Oberpfaffenhofen, Germany

<sup>5</sup> Institute of Environmental Physics, University of Heidelberg, Heidelberg, Germany

<sup>+</sup> now at University of Leeds, Leeds, United Kingdom

<sup>\*</sup> now at Flight Experiments, DLR Oberpfaffenhofen, Germany

Correspondence to M. George ([M.George@leeds.ac.uk](mailto:M.George@leeds.ac.uk)) and M. D. Andrés Hernández ([lola@iup.physik.uni-bremen.de](mailto:lola@iup.physik.uni-bremen.de)).

**Abstract.** In this study, airborne measurements of the sum of hydroperoxyl (HO<sub>2</sub>) and organic peroxy (RO<sub>2</sub>) radicals that react with nitrogen monoxide (NO) to produce nitrogen dioxide, (NO<sub>2</sub>), coupled with actinometry and other key trace gases measurements, have been used to test the current understanding of the fast photochemistry in the outflow of major population centres. The measurements were made during the airborne campaign of the EMeRGe (Effect of Megacities on the transport and transformation of pollutants on the Regional to Global scales) project in Europe on-board the High Altitude Long range research aircraft (HALO). The measurements of RO<sub>2</sub><sup>\*</sup> on HALO were made using the in-situ instrument Peroxy Radical Chemical Enhancement and Absorption Spectrometer (PeRCEAS). RO<sub>2</sub><sup>\*</sup> is to a good approximation the sum of peroxy radicals reacting with NO to produce NO<sub>2</sub>. RO<sub>2</sub><sup>\*</sup> mixing ratios up to 120 pptv were observed in air masses of different origins and composition under different local actinometrical conditions during seven HALO research flights in July 2017 over Europe.

Radical production rates were estimated using knowledge of the photolysis frequencies and the RO<sub>2</sub><sup>\*</sup> precursor concentrations measured on-board, as well as the relevant rate coefficients. Generally, high RO<sub>2</sub><sup>\*</sup> were measured in air masses with high production rates. In the airmasses investigated RO<sub>2</sub><sup>\*</sup> is primarily produced by the reaction of O<sup>1</sup>D with water vapour, and the photolysis of nitrous acid (HONO) and of the oxygenated volatile organic compounds (OVOC, e.g. formaldehyde (HCHO), and glyoxal (CHOCHO)). Due to their short lifetime in most environments, the RO<sub>2</sub><sup>\*</sup> concentrations are expected to be in a photostationary steady state (PSS), i.e., it is assumed a balance between production and loss rates. The RO<sub>2</sub><sup>\*</sup> production and loss rates and the suitability of PSS assumptions to estimate the RO<sub>2</sub><sup>\*</sup> mixing ratios and variability during the airborne observations are discussed. The PSS assumption for RO<sub>2</sub><sup>\*</sup> is considered robust enough to calculate RO<sub>2</sub><sup>\*</sup> mixing ratios for most conditions encountered in the air masses measured. The similarities and discrepancies between measured and PSS calculated RO<sub>2</sub><sup>\*</sup> mixing ratios are discussed. The dominant terminating processes for RO<sub>2</sub><sup>\*</sup> in the pollution plumes measured up to 2000 m are the formation of nitrites and nitrates from radical reactions with NO<sub>x</sub>. Above 2000 m, HO<sub>2</sub> – HO<sub>2</sub> and HO<sub>2</sub> – RO<sub>2</sub> reactions dominate the RO<sub>2</sub><sup>\*</sup> removal. RO<sub>2</sub><sup>\*</sup> calculations by the PSS analytical expression inside the pollution plumes probed often underestimated the measurements. The underestimation is attributed to the limitations of the PSS equation used for the analysis. In particular, this expression does not account for the yields of RO<sub>2</sub><sup>\*</sup> from the oxidation and photolysis of volatile organic compounds, VOCs, and OVOCs other than measured during the EMeRGe research flights in Europe. In air masses with NO mixing ratios ≤ 50 pptv and low VOC/NO ratios, the overestimation of the RO<sub>2</sub><sup>\*</sup> measured observed may be caused by the formation of H<sub>2</sub>O and O<sub>2</sub> from OH and HO<sub>2</sub>, being about 4 times faster than the rate of the OH oxidation reaction of the dominant OVOCs considered.

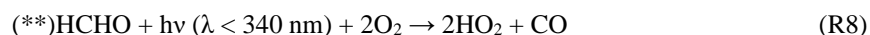
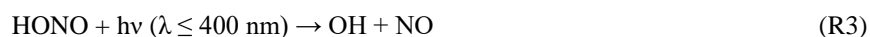
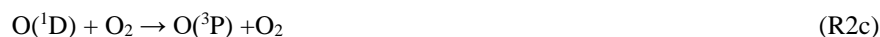
## 40 1. Introduction

Hydroperoxyl (HO<sub>2</sub>) and organic peroxy (RO<sub>2</sub>, where R stands for any organic group) radicals are reactive species that play a key role in the chemistry of the troposphere. In combination with the hydroxyl (OH) radical, HO<sub>2</sub> and RO<sub>2</sub> take part in rapid chemical processes that control the lifetime of many key trace constituents in the troposphere. Examples of key tropospheric processes involving HO<sub>2</sub> and RO<sub>2</sub> are as follows:

- 45 • the catalytic cycles which produce and destroy ozone (O<sub>3</sub>)
- the generation of inorganic acids, which are precursors of aerosol (e.g. sulphuric acid, H<sub>2</sub>SO<sub>4</sub>) and important chemical constituents (e.g. nitric acid, HNO<sub>3</sub>) in both summer and winter smog
- the generation of organic acids; the production of hygroscopic hydrogen peroxide (H<sub>2</sub>O<sub>2</sub>) and organic peroxides (ROOH), which enter aerosol and cloud droplets
- 50 • the generation of organic peroxy nitrates (RO<sub>2</sub>NO<sub>2</sub>), peroxyacetyl nitrate (CH<sub>3</sub>COO<sub>2</sub>NO<sub>2</sub>, PAN) and other summer smog constituents.

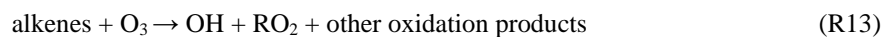
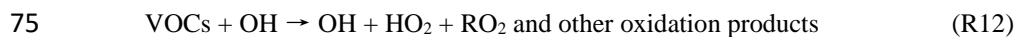
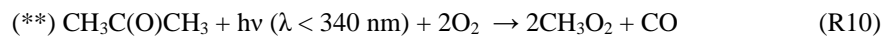
The abundance of HO<sub>2</sub> and RO<sub>2</sub> in the free troposphere has a non-linear and complex dependency on photochemistry, initiated by solar actinic radiation, and on the concentration of the precursors, such as carbon monoxide (CO), volatile organic compounds (VOCs), and peroxides. It also strongly depends on the amounts of nitrogen monoxide (NO) and nitrogen dioxide (NO<sub>2</sub>) due to the gas-phase reactions of NO and NO<sub>2</sub> with the OH and organic oxy (RO) radicals formed during the radical interconversion. The main production and loss processes of HO<sub>2</sub> and RO<sub>2</sub> in the troposphere are summarised as follows:

### a) Production processes of HO<sub>2</sub> and RO<sub>2</sub>



70 (\*) The CH<sub>3</sub> produced from the oxidation of CH<sub>4</sub> or the photolysis of VOCs further reacts with O<sub>2</sub> to form CH<sub>3</sub>O<sub>2</sub>. The net or overall reaction is used, because the formation of CH<sub>3</sub>O<sub>2</sub> is much faster than the CH<sub>3</sub> formation due to the high amount of O<sub>2</sub> present in the atmosphere.

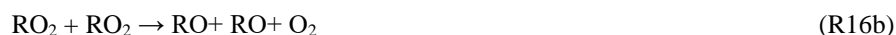
(\*\*) H and CHO formed through the VOC photolysis further react with O<sub>2</sub> to form HO<sub>2</sub>. The net reaction is used, because the formation of HO<sub>2</sub> is much faster than the H and CHO formation due to the high amount of O<sub>2</sub> present in the atmosphere.



b) Loss processes of HO<sub>2</sub> and RO<sub>2</sub>



In addition, HO<sub>2</sub> and RO<sub>2</sub> participate in radical interconversion reactions such as:



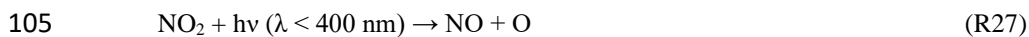
R23 and R25 are two of the most important reactions in the troposphere as they lead to O<sub>3</sub> formation via the reactions R27 and R28. The rate of R22 in the atmosphere compared to that of R26 is negligible.

The sum of HO<sub>2</sub> and RO<sub>2</sub> that react with NO to produce NO<sub>2</sub> can be estimated by assuming that the interconversion of NO to NO<sub>2</sub> reaches a photostationary steady-state (PSS), in which production and loss are to a good approximation equal.

(\*) The CH<sub>3</sub> produced from the oxidation of CH<sub>4</sub> or the photolysis of VOCs further reacts with O<sub>2</sub> to form CH<sub>3</sub>O<sub>2</sub>. The net or overall reaction is used, because the formation of CH<sub>3</sub>O<sub>2</sub> is much faster than the CH<sub>3</sub> formation due to the high amount of O<sub>2</sub> present in the atmosphere.

(\*\*) H and CHO formed through the VOC photolysis further react with O<sub>2</sub> to form HO<sub>2</sub>. The net reaction is used, because the formation of HO<sub>2</sub> is much faster than the H and CHO formation due to the high amount of O<sub>2</sub> present in the atmosphere.

The PSS assumption for  $[\text{NO}_2]$  in the following mechanism (R23 to R29) leads to Eq. 1



$$[\text{HO}_2 + \text{RO}_2]_{\text{PSS}} = \frac{k_{\text{NO}+\text{O}_3}}{k_{\text{NO}+(\text{HO}_2+\text{RO}_2)}} \left( \frac{j_{\text{NO}_2}[\text{NO}_2]}{k_{\text{NO}+\text{O}_3}[\text{NO}]} - [\text{O}_3] \right) \quad (\text{Eq.1})$$

110 where  $j_{\text{NO}_2}$  is the photolysis frequency of  $\text{NO}_2$ ;  $k_{\text{NO}+\text{O}_3}$  ( $1.9 \times 10^{-14} \text{ cm}^3 \text{ molecules}^{-1} \text{ s}^{-1}$  at 298K and 1 atm.) is the rate coefficient of the reaction of  $\text{NO}$  with  $\text{O}_3$  and  $k_{\text{NO}+(\text{HO}_2+\text{RO}_2)}$  is usually estimated for the most abundant peroxy radicals  $\text{HO}_2$  and  $\text{CH}_3\text{O}_2$  by assuming a 1:1  $\text{HO}_2$  to  $\text{CH}_3\text{O}_2$  ratio and averaging the  $k_{\text{NO}+\text{HO}_2}$  ( $8.2 \times 10^{-12} \text{ cm}^3 \text{ molecules}^{-1} \text{ s}^{-1}$  at 298K and 1 atm.) and  $k_{\text{NO}+\text{CH}_3\text{O}_2}$  ( $7.7 \times 10^{-12} \text{ cm}^3 \text{ molecules}^{-1} \text{ s}^{-1}$  at 298K and 1 atm.) rate coefficients for the reaction with  $\text{NO}$ . As noted by Parrish et al. (1986), the PSS assumption requires conditions with sufficient and stable solar irradiation, ensuring  $\text{NO}_2$  stable photolysis rates ( $j_{\text{NO}_2}$ ).

115 The PSS radical calculation made on the assumption of the  $\text{NO}_2$  steady state is very sensitive to the accuracy of the  $\text{NO}_2$  to  $\text{NO}$  ratio and the  $\text{O}_3$  measurements. The comparison of  $[\text{HO}_2 + \text{RO}_2]_{\text{PSS}}$  calculated using Eq.1 with ground-based (e.g. Ridley et al., 1992; Cantrell et al., 1997; Carpenter et al., 1998; Volz-Thomas et al., 2003), and airborne measurements, has shown in the past different degrees of agreement. The underestimations and overestimations found in air masses with different chemical compositions are not well understood. For the case of airborne measurements, the PSS calculation generally overestimates that measured peroxy radicals (Cantrell et al., 2003a, 2003b). The differences observed could not be attributed to systematic changes in  $\text{NO}$ , altitude, water vapour and temperature, although these variables are often correlated.

120 Ground-based (Mihelcic et al., 2003; Kanaya et al., 2007, 2012; Elshorbany et al., 2012; Lu et al., 2012, 2013; Tan et al., 2017, 2018; Whalley et al., 2018, 2021; Lew et al., 2020) and airborne (Crawford et al., 1999; Tan et al., 2001; Cantrell et al., 2003b) measurements have also been compared with model simulations of  $\text{HO}_2$  and  $\text{RO}_2$ . The discrepancies encountered depend upon the chemical composition of the air mass and the chemical mechanisms and constraints used in the model simulations. Tan et al., 2019 and Whalley et al., 2021 reported experimental radical budget calculations using the published reaction rate coefficients of the reactions (R1 to R26), which control  $\text{OH}$ ,  $\text{HO}_2$  and  $\text{RO}_2$  in the lower troposphere, and the ground-based measurements of all relevant reactants and photolysis frequencies. In this study, a similar approach has been used to calculate the amount of peroxy radicals in the air masses measured on-board of the **H**igh **A**ltitude **L**ong range (HALO) research aircraft over Europe during the first campaign of the EMeRGe (**E**ffect of **M**egacities on the transport and transformation of pollutants on the **R**egional to **G**lobal scales) project. The available on-board measurements of  $\text{RO}_2^*$  are defined as the total sum of  $\text{OH}$ ,  $\text{RO}$  and peroxy radicals (i.e.,  $\text{RO}_2^* = \text{OH} + \sum \text{RO} + \text{HO}_2 + \sum \text{RO}_2$ , where  $\text{RO}_2$  are the organic peroxy radicals producing  $\text{NO}_2$  in their reaction with  $\text{NO}$ ). As the amount of  $\text{OH}$  and  $\text{RO}$  is much smaller,  $\text{RO}_2^*$  to a good approximation is the sum of  $\text{HO}_2$  and those  $\text{RO}_2$  radicals that react with  $\text{NO}$  to produce  $\text{NO}_2$ . For the calculation,  $\text{RO}_2^*$  is assumed to be in PSS, and an analytical expression is developed with a manageable degree of complexity to estimate the concentration and mixing ratios of  $\text{RO}_2^*$ . The simultaneous on-board measurements of trace  
135 gases and photolysis frequencies are used to constrain the estimate of the  $\text{RO}_2^*$  concentration.

In contrast to other experimental deployments, the concentrations and/or mixing ratios of the majority of the key species involved in reactions R1 to R26 were continuously measured on-board HALO during the EMerGe campaign. This enables the use of a large number of measurements to constrain the PSS calculation of  $\text{RO}_2^*$ . Consequently, this data set provides an excellent opportunity to gain deeper insight into the source and sink reactions of  $\text{RO}_2^*$  and the applicability of the PSS assumption for the different pollution regimes and related weather conditions in the free troposphere.

140

## 2. EMerGe field campaign in Europe

The overarching objective of the EMerGe project is to test and improve the current understanding of the photochemical and heterogeneous processing of pollution outflows from major population centres (MPCs) and their impact on the atmosphere. Two intensive observational periods (IOP) were carried out to investigate selected European and Asian MPC outflows. The European IOP took place from 10 to 28 July 2017 (<http://www.iup.uni-bremen.de/emerge/home/home.html>). An extensive set of in-situ and remote-sensing airborne measurements of trace gases and aerosol particles were made on-board the HALO aircraft (see [www.halo-spp.de](http://www.halo-spp.de)) along flight tracks in the lower layers of the troposphere from northwest Europe to the Mediterranean region.

145

During EMerGe in Europe, HALO made a total of 53 flight hours distributed over seven flights to investigate the chemical composition of the outflows from the target MPCs: London, Paris, Benelux/ Ruhr metropolitan area, Po Valley, and urban agglomerations such as Rome, Madrid, and Barcelona. The flight tracks are shown in Fig. 1. All HALO flights started from the HALO base at the DLR in Oberpfaffenhofen, southwest of Munich, Germany. To achieve the scientific goals, 60 % of the flights flew at altitudes below 3000 m. Vertical profiles of trace constituents were typically made by keeping the HALO altitude constant at different flight levels upwind and downwind of the target MPCs. The flights are named E-EU-FN, where E stands for EMerGe, EU for Europe, and FN is the two-digit flight number. More details about the EMerGe IOP in Europe and the set of instruments deployed on-board the HALO aircraft are described elsewhere (Andrés Hernández et al., 2022).

150

155

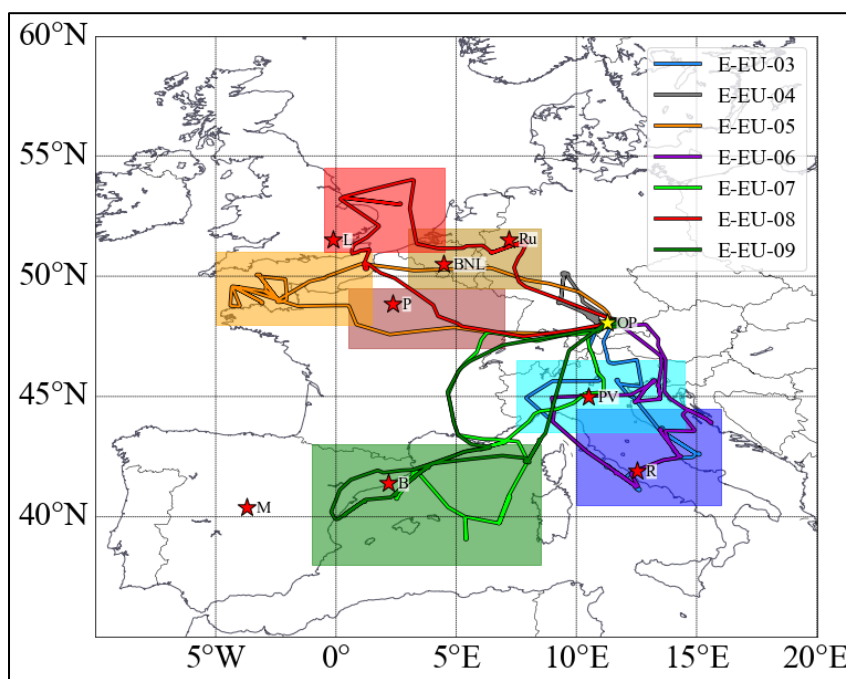


Figure 1: The research flight tracks made by HALO during the EMerGe-Europe campaign on 11, 13, 17, 20, 24, 26 and 28 July 2017 (E-EU-03 to E-EU-09, respectively, colour coded). MPC target areas are colour coded by shading, and the targeted locations/regions are marked with red stars, M: Madrid, B: Barcelona, P: Paris, L: London; BNL: BeNeLux; Ru: Ruhr area; PV: Po Valley, R: Rome. The location of the HALO base at the DLR in Oberpfaffenhofen, Germany (OP) is indicated by a yellow star.

160

### 3. PeRCEAS and other instruments on-board HALO during EMERGe

The  $\text{RO}_2^*$  measurements on-board the HALO research aircraft during EMERGe were made using the Peroxy Radical Chemical Enhancement and Absorption Spectrometer (PeRCEAS). PeRCEAS combines the Peroxy Radical Chemical Amplification (PeRCA) and Cavity Ring-Down Spectroscopy (CRDS) techniques in a dual-channel instrument. Each channel has a separate chemical reactor and detector, which operate alternatively in both background and amplification modes to account for the rapid background variations during airborne measurements. In both modes NO is continuously added to the air sampled at the reactor, while CO is only added in the amplification mode to initiate the chain conversion of  $\text{RO}_2^*$  into  $\text{NO}_2$ . In the amplification mode, the sum of the  $\text{NO}_2$  produced from ambient  $\text{RO}_2^*$  through the chain reaction, the ambient  $\text{NO}_2$ , the  $\text{NO}_2$  produced from the ambient  $\text{O}_3 - \text{NO}$  reagent gas reaction and the  $\text{NO}_2$  produced in the inlet from any other sources (e.g. thermal decomposition of PAN) is measured. In the background mode, the sum of the ambient  $\text{NO}_2$ , the  $\text{NO}_2$  produced from the ambient  $\text{O}_3 - \text{NO}$  reagent gas reaction and  $\text{NO}_2$  produced in the inlet from any other sources is measured. The  $\text{RO}_2^*$  is retrieved by dividing the difference in  $\text{NO}_2$  concentration ( $\Delta\text{NO}_2$ ) between amplification and background mode by the conversion efficiency of  $\text{RO}_2^*$  to  $\text{NO}_2$ , which is referred to as eCL (effective chain length). The PeRCEAS instrument and its specifications have been described in detail elsewhere (Horstjann et al., 2014, George et al., 2020).

The two chemical reactors for sampling the ambient air are part of the DUAL channel Airborne peroxy radical Chemical Amplifier (DUALER) inlet installed inside a pylon located on the outside of the HALO fuselage. During the EMERGe campaign in Europe, a reagent gas mixing ratio of 30 ppmv NO ( $[\text{NO}] = 1.46 \times 10^{14}$  molecules  $\text{cm}^{-3}$  at 296 K, 200 mbar) and of 9 % CO ( $[\text{CO}] = 4.4 \times 10^{17}$  molecules  $\text{cm}^{-3}$  at 296 K, 200 mbar) were added to the sample flow for the chemical conversion of  $\text{RO}_2^*$  to  $\text{NO}_2$ . The DUALER inlet was operated at an internal pressure of 200 mbar to achieve stable chemical conversion. The  $\text{HO}_2$  and  $\text{RO}_2$  detection sensitivity depends on the rates of loss of  $\text{HO}_2$  and  $\text{RO}_2$  by the R19 and R22 reactions. The latter depend on the concentration of the reagent gas NO added and the reactions rate coefficients, where  $k_{22}$  is larger than  $k_{19}$ . The average eCL for a 1:1  $\text{HO}_2$  to  $\text{CH}_3\text{O}_2$  mixture under the DUALER conditions during the campaign in Europe was determined to be  $50 \pm 8$  from laboratory calibrations, where the error is the  $\pm 1\sigma$  standard deviation estimated from the reproducibility of the experimental determinations. Likewise, the ratio  $\alpha = \text{eCL}_{\text{CH}_3\text{O}_2} / \text{eCL}_{\text{HO}_2}$  was determined to be 65% for the measurement conditions (George et al., 2020). The values obtained from calibrations before and after the campaign agreed within their experimental errors.

Although the DUALER pressure is kept constant below the ambient pressure, variations in dynamical pressure  $> 10$  mbar during the flight change the residence time and induce turbulences inside the inlet (Kartal et al., 2010; George et al., 2020). These may lead to different physical losses of radicals before amplification and affect the eCL. In the measurements presented in this study, variations in dynamical pressure of this magnitude were only encountered during flight level changes of the aircraft. When used during the analysis, these data sets are either excluded or flagged (P\_flag). The effect of the ambient air humidity on eCL (Mihele and Hastie, 1998; Mihele et al., 1999; Reichert et al., 2003) has been accounted for by a calibration procedure reported in George et al. (2020). The  $[\text{H}_2\text{O}]$  in the DUALER inlet was lower than  $1 \times 10^{17}$  molecules  $\text{cm}^{-3}$  for 60 % of measurements during EMERGe in Europe, for which the  $\text{eCL}_{\text{wet}} = 76$  % of  $\text{eCL}_{\text{dry}}$ . At the highest humidity observed during the campaign, i.e.,  $[\text{H}_2\text{O}]_{\text{inlet}} = 2 \times 10^{17}$  molecules  $\text{cm}^{-3}$ , the  $\text{eCL}_{\text{wet}}$  is 55 % of  $\text{eCL}_{\text{dry}}$  (see Fig. S1 in the supplementary information).

In addition to the measurement of  $\text{RO}_2^*$  from PeRCEAS, other in-situ and remote-sensing measurements and basic aircraft data from HALO are used in this study. Details of the corresponding instruments are summarised in Table 1. The remote sensing instruments used on HALO during EMERGe were the mini Differential Optical Absorption (miniDOAS) and the Heidelberg Airborne Imaging DOAS Instrument (HAIDI). The miniDOAS observes the atmosphere using six telescopes: two being optimised

for the ultraviolet, two for the visible, and two for the near infrared. Three telescopes observe in nadir viewing and three in limb  
 200 viewing. The three limb scanning telescopes point to the starboard side perpendicular to the aircraft fuselage axis. They are rotated  
 to compensate for roll relative to the horizon. A variant of the DOAS retrieval technique uses least square fitting of the measured  
 and radiative transfer modelled absorption along the line of sight to retrieve the differential Slant Column Density (dSCD) of the  
 target gas and a scaling reference gas. The latter is the dimer of molecular oxygen ( $O_4$ ). As the vertical profile of the concentrations  
 of  $O_2$  and thus  $O_4$  are known then the mixing ratios of the target gas at the flight altitude is obtained from the target gas and  $O_4$   
 205 dSCDs (for more details see Stutz et al., 2017; Hüneke et al., 2017; Kluge et al., 2020; Rotermund et al., 2021). The HAIDI nadir  
 observations are used to retrieve dSCDs below the aircraft. The dSCDs from HAIDI are then converted to mixing ratios using  
 knowledge of the aircraft altitude and the corresponding geometric Air Mass Factor (AMF), calculated by a radiative transfer  
 model under a well-mixed  $NO_2$  layer assumption. As a result of this assumption, the calculated mixing ratios for HAIDI target  
 gases are lower limits and similar to the actual values while flying within and close to a well-mixed boundary layer. In spite of the  
 210 differences in sampling volume and temporal and spatial resolution between the in-situ and remote sensing measurement  
 techniques, the concentration of the gas HCHO measured by both techniques were in good agreement and the concentrations of  
 the  $NO_2$  (remote sensing) and  $NO_y$  (in situ) were consistent (for more details see Schumann, 2020).

Table 1: List of the airborne measurements and instrumentation used in this study. PeRCA: Peroxy Radical Chemical Amplification;  
 CRDS: Cavity Ring-Down Spectroscopy; PTR-MS: Proton-Transfer-Reaction Mass Spectrometer; AT-BS: Adsorption Tube and Bag air  
 215 Sampler; TD-GC-MS: Thermal Desorption Gas Chromatography and Mass Spectrometry; DOAS: Differential Optical Absorption Spectrometry;  
 Univ: University; KIT: Karlsruher Institut für Technologie; DLR: Deutsches Zentrum für Luft- und Raumfahrt; IPA: Institut für Physik der  
 Atmosphäre; FZ: Forschungszentrum; FX: Flugexperimente.

<b>Trace gas-in situ measurements</b>				
Species/parameters	Acronym	Institution	Technique/Instrument	Reference
$RO_2^* = HO_2 + \sum RO_2$	PeRCEAS	Univ. Bremen	PeRCA + CRDS	George et al., 2020
OVOC	HKMS	KIT Karlsruhe	PTR-MS	Brito and Zahn, 2011
$O_3$	FAIRO	KIT Karlsruhe	UV-Photometry/ Chemiluminescence	Zahn et al., 2012
$O_3$ , CO	AMTEX	DLR-IPA	UV-Photometry/ VUV-Fluorimetry	Gerbig et al., 1996
NO, $NO_y$	AENEAS	DLR-IPA	Chemiluminescence/ Gold converter	Ziereis et al., 2004
$CO_2$ , $CH_4$	CATS	DLR-IPA	CRDS	Chen et al., 2010
<b>Trace gas- remote sensing measurements</b>				
Species/parameters	Acronym	Institution	Technique/Instrument	Reference
$NO_2$ , HONO, $CH_2O$ , $C_2H_2O_2$ , $C_3H_4O_2$	miniDOAS	Univ. Heidelberg	DOAS / UV-nIR; 2D optical spectrometer	Hüneke et al., 2017
$NO_2$	HAIDI	Univ. Heidelberg	DOAS / 3x2D-imaging spectrometers	General et al., 2014
<b>Other parameters</b>				
Species/parameters	Acronym	Institution	Technique/Instrument	Reference
Spectral actinic flux density (up/down) Photolysis frequencies	HALO-SR	FZ Jülich	CCD spectro- radiometry	Bohn and Lohse, 2017

## 4. Results and discussion

### 4.1. Airborne RO<sub>2</sub><sup>\*</sup> measurements during EMeRGe in Europe

220 RO<sub>2</sub><sup>\*</sup> mixing ratios up to 120 pptv were measured during the campaign, as shown in Fig. 2. Typically, the highest RO<sub>2</sub><sup>\*</sup> mixing ratios were observed below 3000 m over Southern Europe.

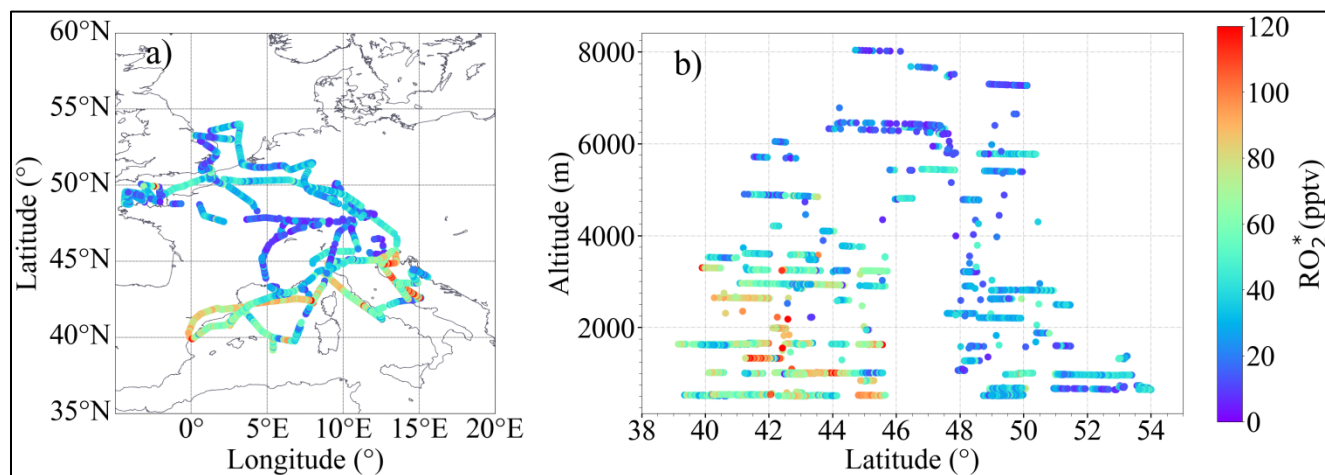
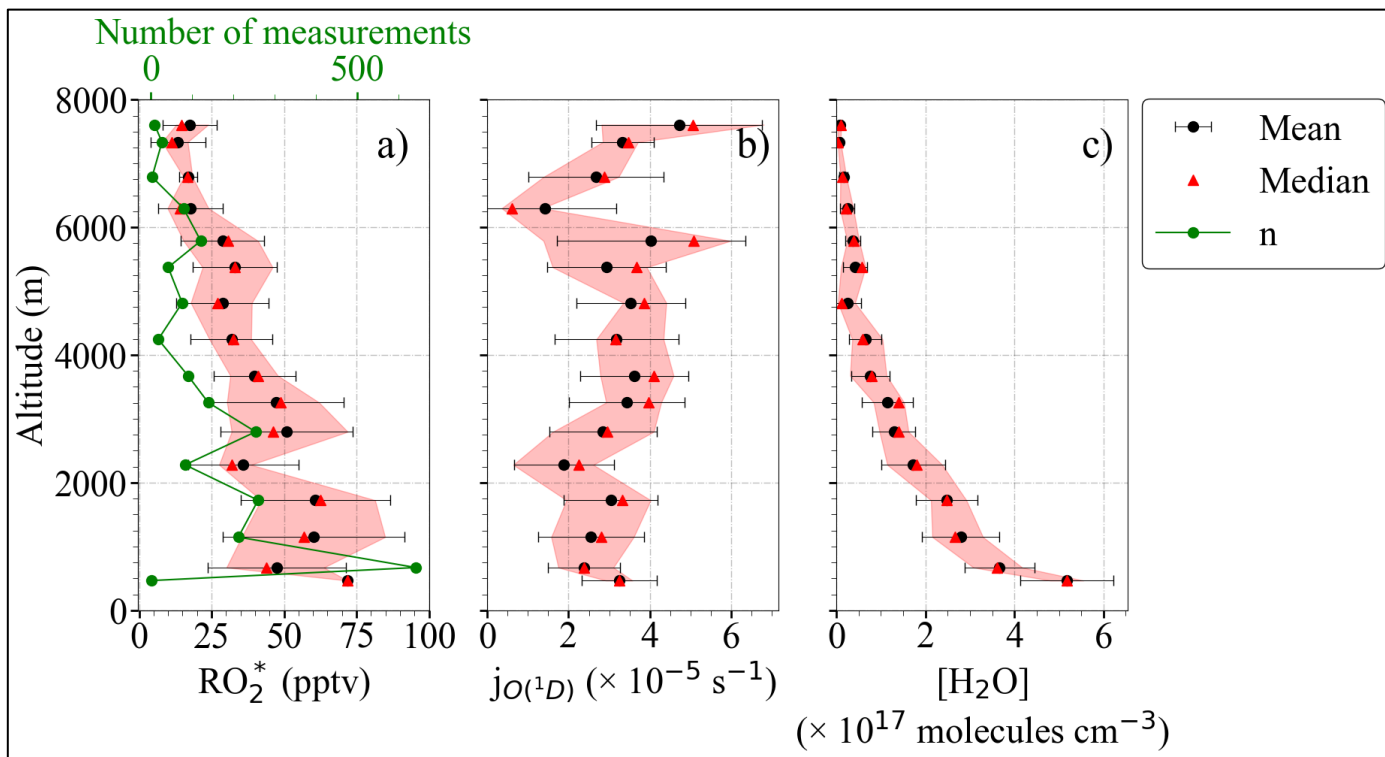


Figure 2: RO<sub>2</sub><sup>\*</sup> measured during EMeRGe-Europe: a) as a function of longitude and latitude, b) as a function of latitude and altitude.

225 The origin and thus the composition of the air sampled during the seven flights over Europe were different and heterogeneous. Typically, the air masses measured were influenced by emissions from MPCs and their surroundings, and sometimes by biomass burning transported over short or long distances. The concentration and mixing ratio of RO<sub>2</sub><sup>\*</sup> rather depends on the insolation and the chemical composition of the air probed, particularly on the abundance of RO<sub>2</sub><sup>\*</sup> precursors, than on the origin of the air masses. Since RO<sub>2</sub><sup>\*</sup> are controlled by fast chemical and photochemical processes, the air mass origin and trajectory are not used in the  
 230 calculation of RO<sub>2</sub><sup>\*</sup> concentrations and mixing ratios but are of interest as the source of RO<sub>2</sub><sup>\*</sup> precursors. Thus, the RO<sub>2</sub><sup>\*</sup> variability and its production rates provide valuable insight into the photochemical activity of the air masses probed.

Changes in RO<sub>2</sub><sup>\*</sup> as a function of latitude and altitude, as shown in Fig. 2, confirm the heterogeneity of the photochemical activity in the air masses probed. Figure 3 shows the RO<sub>2</sub><sup>\*</sup> vertical profiles averaged for the EMeRGe flights over Europe in 500 m altitude bins. The error bars are standard errors (i.e.  $\pm 1\sigma$  standard deviation of each bin). The vertical profiles may be biased as the higher altitudes have fewer measurements than those below 3000 m, as mentioned in section 2. The vertical profiles are a composite from  
 235 averaging flights with legs carried out at different longitude and latitudes, and are only shown to summarise the variability in the composition of the air masses measured during the campaign.





240 Figure 3: Composite average vertical profiles of a)  $RO_2^*$ , b)  $j_{O(^1D)}$  and c)  $[H_2O]$  observations. The measurements are binned over 500 m altitude. The error bars are the  $\pm 1\sigma$  standard deviation of each bin. Median values (red triangles) the interquartile 25-75% range (red-shaded area) and the number of individual measurements,  $n$ , for each bin (in green) are additionally plotted.

Most of the EMeRGe measurements below 2000 m were carried out in the outflow of MPCs, which are expected to contain significant amounts of  $RO_2^*$  precursors. HALO flew at the lowest altitudes during flight legs over the English Channel, the Mediterranean and the North Sea. The  $H_2O$  concentration in the air masses decreases steadily with altitude as expected. The higher relative variability in  $H_2O$  observed at 3000 m and the increase at 5000 m is associated with measurements under stormy conditions, often over the Alps.

#### 4.2. $RO_2^*$ production rates

The rate of production of  $RO_2^*$  from the reactions R1 to R13 is given by:

$$\begin{aligned}
 P_{RO_2^*} = & 2j_{O_D^1}[O_3] \frac{k_{O_D^1+H_2O}[H_2O]}{k_{O_D^1+H_2O}[H_2O] + k_{O_D^1+O_2}[O_2] + k_{O_D^1+N_2}[N_2]} + j_{HONO}[HONO] + 2j_{H_2O_2}[H_2O_2] + 2\sum_i j_i[OVOC_i] + \\
 & + \sum k_{O_3+alkenes_k}[O_3][alkenes_k] \quad (\text{Eq. 2})
 \end{aligned}$$

where OVOC stands for oxygenated volatile organic compounds.

In this study, Eq. 2 has been applied to the measurements taken within the EMeRGe campaign in Europe. There were no  $H_2O_2$  measurements available for EMeRGe. However, the results reported by Tan et al. (2001), indicate that the rate of OH production from the  $H_2O_2$  photolysis is not significant except when  $NO_x$  is low. To be more precise, for conditions having  $NO < 50$  ppt, the partitioning of  $HO_x$  is strongly shifted to  $HO_2$ .  $HO_2$  then predominantly reacts with itself or  $RO_2$  to form peroxides, which can in turn photolyse. For conditions with  $NO > 50$  pptv the rates of reactions of  $HO_x$  with  $NO_x$  are faster than those of  $HO_2$  with  $HO_2$

and RO<sub>2</sub>. As the NO mixing ratio was higher than 50 pptv in 75 % of the air masses probed in Europe, the rate of the photolysis of H<sub>2</sub>O<sub>2</sub> was as a first approximation assumed not to be significant source of OH for the EMeRGe dataset considered in this study.

Formaldehyde (HCHO), acetaldehyde (CH<sub>3</sub>CHO), acetone, (CH<sub>3</sub>C(O)CH<sub>3</sub>), and glyoxal (CHOCHO) were the OVOCs measured in EMeRGe forming directly radicals through photolysis. They are produced in the photolysis and oxidation of VOCs and are likely the most abundant and reactive OVOCs present. In this study they were assumed to be the dominant VOCs in the air masses probed.

There were no measurements of alkenes provided in EMeRGe. Consequently the ozonolysis term in Eq. 2 was not included in the analysis.

The above assumptions lead to Eq. 3, which calculates the RO<sub>2</sub><sup>\*</sup> production rate (P<sub>RO<sub>2</sub><sup>\*</sup></sub>) for the EMeRGe measurements as follows:

$$P_{RO_2^*} = 2j_{O(^1D)}[O_3] \frac{k_{O_D + H_2O} [H_2O]}{k_{O_D + H_2O} [H_2O] + k_{O_D + O_2} [O_2] + k_{O_D + N_2} [N_2]} + j_{HONO} [HONO] + 2j_{HCHO} [HCHO] + 2j_{CH_3CHO} [CH_3CHO] + 2j_{CH_3C(O)CH_3} [CH_3C(O)CH_3] + 2j_{CHOCHO} [CHOCHO] \quad (\text{Eq.3})$$

The production rate of RO<sub>2</sub><sup>\*</sup> molecules can be expressed in units of mixing ratio of RO<sub>2</sub><sup>\*</sup> by dividing with the air concentration at each altitude, calculated from the pressure and temperature measurements (for the vertical profile and the latitudinal distribution of P<sub>RO<sub>2</sub><sup>\*</sup></sub> see Fig. S2 and S3 in the supplementary information). Figure 4 shows the composite averaged vertical profile of all measured RO<sub>2</sub><sup>\*</sup> mixing ratios colour-coded with the calculated P<sub>RO<sub>2</sub><sup>\*</sup></sub>. For the sake of representativeness and comparability, the number of measurements in each altitude bin is shown in Fig. 4b. The higher RO<sub>2</sub><sup>\*</sup> mixing ratios observed below 4000 m are typically associated with P<sub>RO<sub>2</sub><sup>\*</sup></sub> ≥ 0.4 pptv s<sup>-1</sup>. Above 4000 m both P<sub>RO<sub>2</sub><sup>\*</sup></sub> and RO<sub>2</sub><sup>\*</sup> start to decrease with altitude, as expected. This is related to the decrease in H<sub>2</sub>O and other radical precursor concentrations with altitude, as detailed in Fig. 5 and Fig. 6. In previous airborne campaigns at various parts of the world, RO<sub>2</sub><sup>\*</sup> vertical distributions showed a local maximum between 1500 and 4000 m, as reported by Tan et al. (2001), Cantrell et al. (2003a, 2003b), and Andrés-Hernández et al. (2009). In the present work, this local maximum is more evident for measurements with P<sub>RO<sub>2</sub><sup>\*</sup></sub> ≥ 0.5 pptv s<sup>-1</sup>.

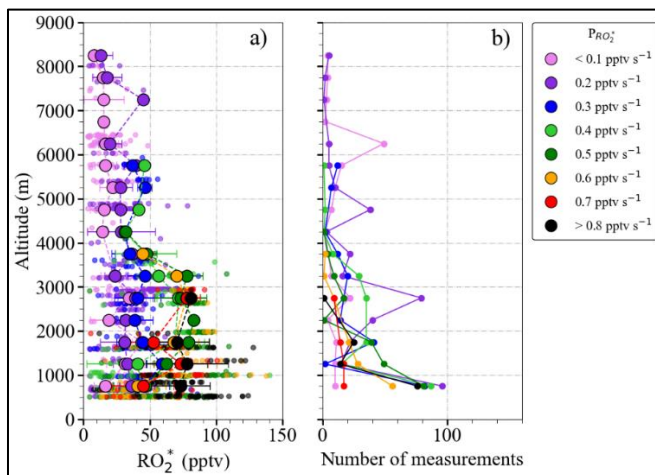


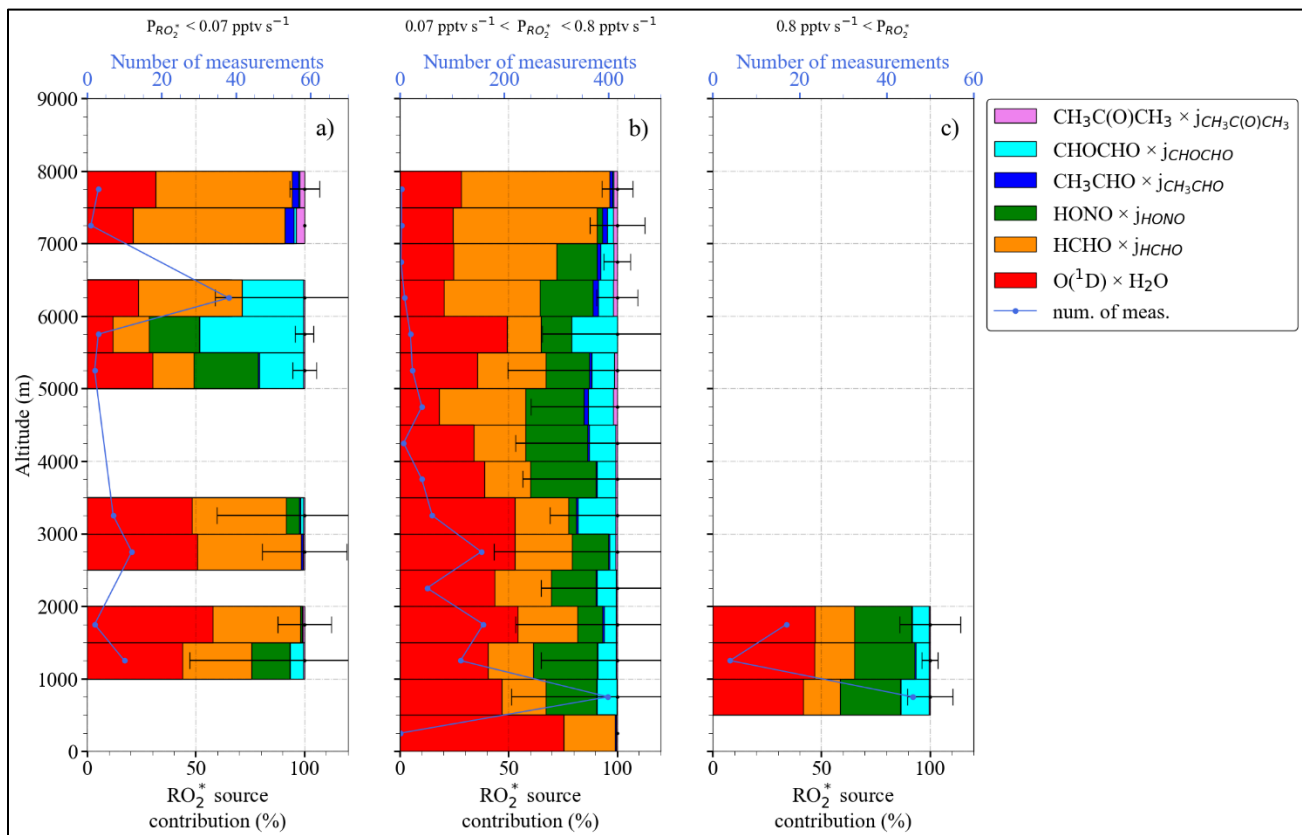
Figure 4: a) Composite averaged vertical distribution of measured RO<sub>2</sub><sup>\*</sup> colour-coded according to the value of P<sub>RO<sub>2</sub><sup>\*</sup></sub>, b) the number of measurements in each altitude bin. Small circles are 1-minute individual measurements binned with P<sub>RO<sub>2</sub><sup>\*</sup></sub> values in 0.1 pptv s<sup>-1</sup> intervals. Larger circles result from a further binning over 500 m altitude steps. All the production rates below 0.1 pptv s<sup>-1</sup> and above 0.8 pptv s<sup>-1</sup> are binned to 0.1 pptv s<sup>-1</sup> and 0.8 pptv s<sup>-1</sup>, respectively. The error bars are the standard deviation for each altitude bin.

Figure 5 shows the fractional contribution of the production rate from each radical precursor reaction included in Eq. 3 as a function of altitude. The data are classified into three groups according to the rate of change of production of the  $\text{RO}_2^*$  mixing ratio  $P_{\text{RO}_2^*} < 0.07 \text{ pptv s}^{-1}$  (5a),  $0.07 < P_{\text{RO}_2^*} < 0.8 \text{ pptv s}^{-1}$  (5b), and  $P_{\text{RO}_2^*} > 0.8 \text{ pptv s}^{-1}$  (5c) to show the lowest, most common, and highest ranges, respectively, encountered during the campaign. For 89 % of the measurements,  $0.07 < P_{\text{RO}_2^*} < 0.8 \text{ pptv s}^{-1}$  applies, while the rest of the data are equally distributed in the other two  $P_{\text{RO}_2^*}$  ranges. The data in each group are always binned over 500 m when available.

Typically, the high amount of  $\text{H}_2\text{O}$  in the air masses probed leads to the reaction of  $\text{O}^1\text{D}$  with  $\text{H}_2\text{O}$  (R1-R2a) being the highest  $\text{RO}_2^*$  radical production rate ( $\geq 50 \%$ ) below 4000 m. As the amount of  $\text{H}_2\text{O}$  reduces with altitude, the relative contribution from  $\text{O}_3$  photolysis decreases. Above 4000 m,  $\text{HCHO}$ ,  $\text{HONO}$ , and  $\text{CHOCHO}$  photolysis contributions range between 20 % to 40 %, 2.5 % to 30 %, and 5 % to 25 %, respectively. The  $\text{HCHO}$  contribution increases up to 80% during measurements above 6000 m. The contributions of  $\text{CH}_3\text{CHO}$  and  $\text{CH}_3\text{C}(\text{O})\text{CH}_3$  photolysis are, in contrast, practically negligible ( $< 5 \%$ ).

The vertical changes of the precursor mixing ratios and photolysis frequencies used to calculate  $P_{\text{RO}_2^*}$  in Fig. 5 are shown in Fig. 6a to 6f.  $P_{\text{RO}_2^*} < 0.07 \text{ pptv s}^{-1}$  is associated with measurements under cloudy conditions, towards sunset where the photolysis frequencies are low, or at altitudes above 5000 m in air masses with a low amount of  $\text{RO}_2^*$  precursors.  $P_{\text{RO}_2^*} > 0.8 \text{ pptv s}^{-1}$  are found for air masses, measured below 2000 m in the outflow of MPCs over the sea, for conditions having sufficient insolation ( $j_{\text{O}^1\text{D}} > 3 \times 10^{-5} \text{ S}^{-1}$ ) and a high content of  $\text{RO}_2^*$  precursors ( $\text{HCHO} > 1000 \text{ pptv}$  and  $\text{HONO} > 100 \text{ pptv}$ ). The increase in the photolysis frequencies as a function of altitude is concurrent with decreases in precursor concentrations. As a result, the  $P_{\text{RO}_2^*}$  do not significantly vary with altitude in the air masses investigated.

In previous airborne campaigns, Tan et al. (2001) and Cantrell et al. (2003b) reported a reduction of the fractional contribution of the reaction of  $\text{O}^1\text{D}$  with  $\text{H}_2\text{O}$  as the  $P_{\text{RO}_2^*}$  value decreases. At very low  $P_{\text{RO}_2^*}$  values ( $< 0.03 \text{ pptv s}^{-1}$ ), the sum of all other production terms exceeded the fraction from the  $\text{O}^1\text{D} + \text{H}_2\text{O}$  term. For these conditions,  $\text{H}_2\text{O}_2$  and VOCs photolysis dominated the  $P_{\text{RO}_2^*}$ . For the EMERGe data set in Europe, only 6 % of  $P_{\text{RO}_2^*}$  are below  $0.06 \text{ pptv s}^{-1}$ .



310 Figure 5: Total  $P_{RO_2^*}$  and fractional precursor contributions estimated using Eq. 5 as a function of altitude, for: a)  $P_{RO_2^*} < 0.07$  pptv  $s^{-1}$ , b)  $0.07$  pptv  $s^{-1} < P_{RO_2^*} < 0.8$  pptv  $s^{-1}$ , and c)  $P_{RO_2^*} > 0.8$  pptv  $s^{-1}$ . Note the different scales in the number of measurements.

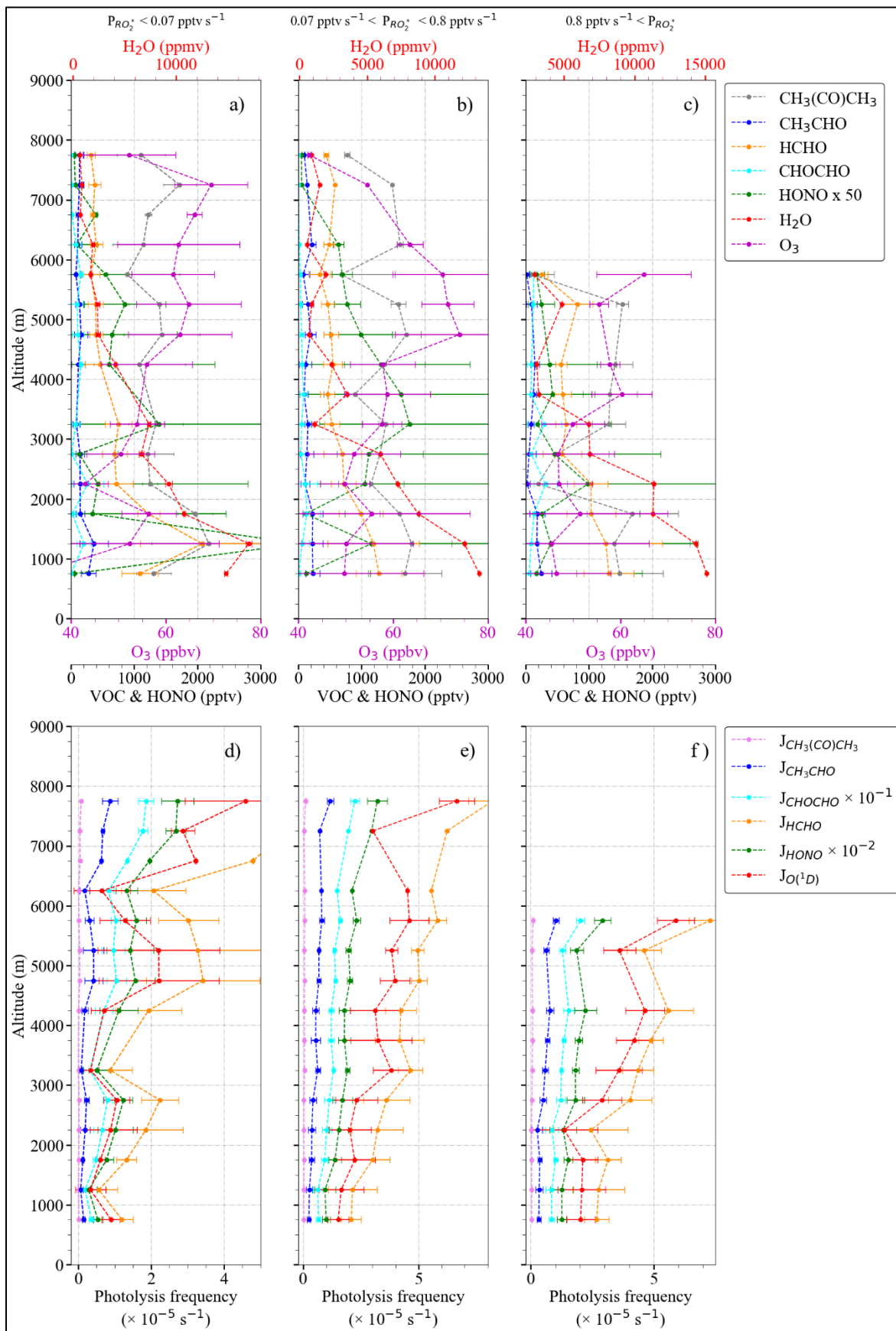


Figure 6: Vertical distribution and variation of a) to c) precursor mixing ratios; d) to f) photolysis frequencies for the  $P_{RO_2}$  bins as in Fig. 5. Note the different scales in the  $H_2O$  concentration

315 **4.3. PSS estimation of the RO<sub>2</sub><sup>\*</sup> mixing ratios**

Under most ambient conditions in the troposphere, the RO<sub>2</sub><sup>\*</sup> are short-lived, and the chemical lifetime of RO<sub>2</sub><sup>\*</sup> is much shorter than the chemical transport time into and out of an air mass being probed. Consequently, pseudo-steady-state conditions prevail, and the radical production and destruction rates are balanced:

320  $P_{RO_2^*} = D_{RO_2^*}$  (Eq.4)

The R5 to R7, R12, R16b, and R23 to R26 are interconversion reactions between OH, RO, HO<sub>2</sub> and RO<sub>2</sub> and do consequently occur without radical losses. Solving Eq. 4 leads to Eq. 5 if RO<sub>2</sub><sup>\*</sup> – RO<sub>2</sub><sup>\*</sup> reactions are assumed to be the dominant radical terminating processes.

325 
$$2j_{O(^1D)}[O_3] \frac{k_{O_b^1+H_2O}[H_2O]}{k_{O_b^1+H_2O}[H_2O] + k_{O_b^1+O_2}[O_2] + k_{O_b^1+N_2}[N_2]} + j_{HONO}[HONO] + 2j_{HCHO}[HCHO] + 2j_{CH_3CHO}[CH_3CHO] + 2j_{CH_3C(O)CH_3}[CH_3C(O)CH_3] + 2j_{CHOCHO}[CHOCHO] = k_{RO_2^*+RO_2^*}[RO_2^*]^2$$
 (Eq. 5)

where  $j_{HCHO}$ ,  $j_{CH_3CHO}$ ,  $j_{CH_3C(O)CH_3}$ ,  $j_{CHOCHO}$  are respectively  $j_8$ ,  $j_9$ ,  $j_{10a,b}$  and  $j_{11}$ , as in Table 1 in the supplementary information. and  $k_{RO_2^*+RO_2^*}$  represents an effective RO<sub>2</sub><sup>\*</sup> self-reaction rate coefficient, comprising HO<sub>2</sub> – HO<sub>2</sub>, HO<sub>2</sub> – RO<sub>2</sub> and RO<sub>2</sub> – RO<sub>2</sub> reaction rates.

330 Consequently, the RO<sub>2</sub><sup>\*</sup> concentrations are expected to correlate with the square root of the  $P_{RO_2^*}$ .

Figure 7 shows the relationship between the measured [RO<sub>2</sub><sup>\*</sup>] and the calculated  $\sqrt{P_{RO_2^*}}$ . Generally, both [RO<sub>2</sub><sup>\*</sup>] and  $\sqrt{P_{RO_2^*}}$  increase with the photolysis frequency of O<sub>3</sub> ( $j_{O(^1D)}$ ). Measurements in which [RO<sub>2</sub><sup>\*</sup>] were less than  $0.5 \times 10^{12}$  molecules cm<sup>-3</sup>,  $\sqrt{P_{RO_2^*}}$  less than 1000 and with  $j_{O(^1D)} > 5 \times 10^{-5}$  were made above 6000 m, where the amount of RO<sub>2</sub><sup>\*</sup> precursors is low. The relatively weak correlation observed between [RO<sub>2</sub><sup>\*</sup>] and  $\sqrt{P_{RO_2^*}}$  indicates the necessity of other radical terminating processes and/or missing radical formation terms in the  $P_{RO_2^*}$  calculation. Apart from this, the spread in the diagram confirms that the effective RO<sub>2</sub><sup>\*</sup> self-reaction rate  $k_{RO_2^*+RO_2^*}[RO_2^*]^2$  varies widely in the air masses probed likely due to the effect of changes in HO<sub>2</sub> and  $\Sigma RO_2$  concentrations in the individual loss reaction rate coefficients. Photochemical processing is expected to be enhanced over Southern Europe due to the prevailing conditions of high insolation and temperatures during the EMERGe flights, which might lead to the rapid production of RO<sub>2</sub><sup>\*</sup> from the photochemical oxidations of CO and VOCs. This is also reflected in the higher  $P_{RO_2^*}$  and [RO<sub>2</sub><sup>\*</sup>] observed in Southern Europe as compared to those in Northern Europe (Fig. 7b).

335  
340

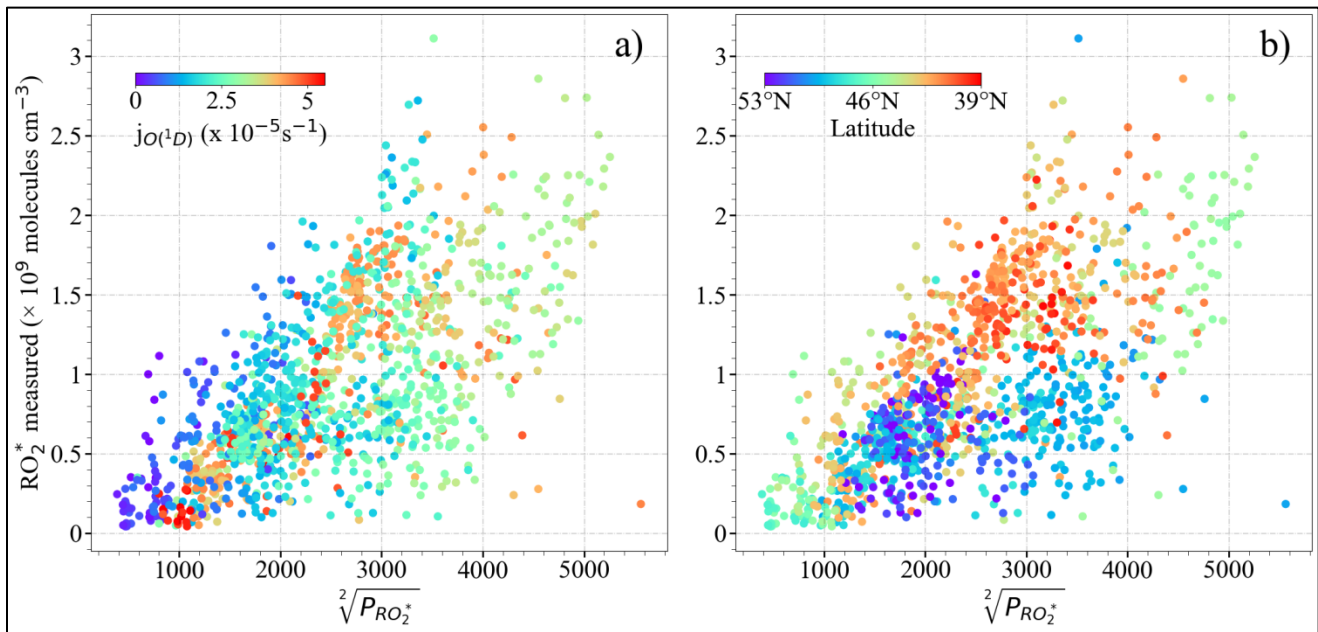
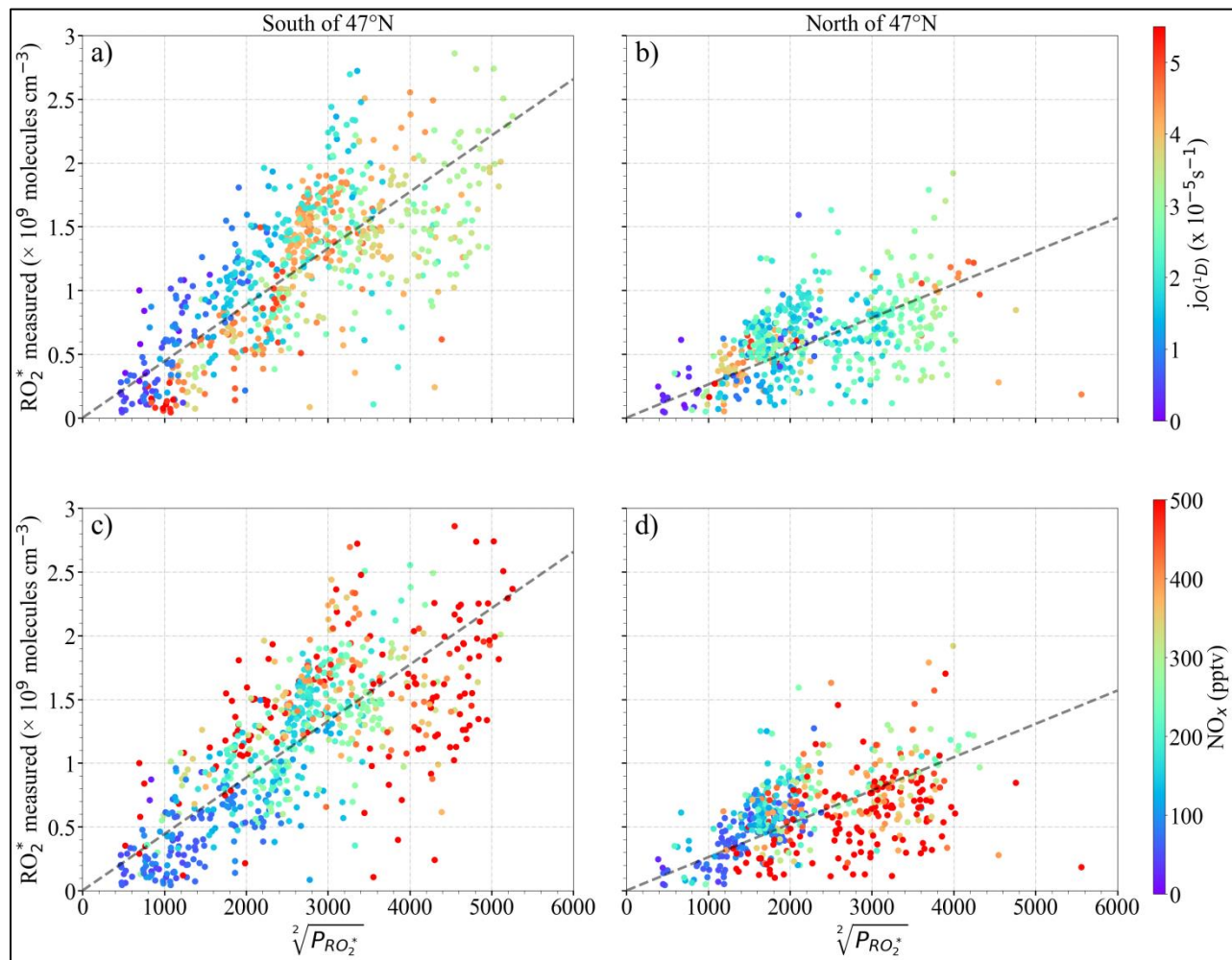


Figure 7: Measured  $[\text{RO}_2^*]$  versus calculated  $\sqrt{P_{\text{RO}_2^*}}$  colour-coded for values of a)  $j_{\text{O}(^1\text{D})}$  and b) latitude.

The correlation between  $[\text{RO}_2^*]$  and  $\sqrt{P_{\text{RO}_2^*}}$  improves when the measurements south and north of  $47^\circ\text{N}$  are separately analysed (Fig. 8). For a given  $[\text{RO}_2^*]$ , the  $P_{\text{RO}_2^*}$  calculated is higher for the measurements north of  $47^\circ\text{N}$  than south of  $47^\circ\text{N}$ . The lowest  $[\text{RO}_2^*]$  to  $\sqrt{P_{\text{RO}_2^*}}$  ratios are associated with higher  $\text{NO}_x$  ( $\text{NO} + \text{NO}_2$ ), especially north of  $47^\circ\text{N}$ , indicating the urban character and higher amounts of the  $\text{RO}_2^*$  precursors of the air probed (Fig. 8d). Please note that these results are only valid for the data set acquired over Europe during EMeRGe flights and do not yield a relationship between  $[\text{RO}_2^*]$  and  $\sqrt{P_{\text{RO}_2^*}}$ , which is generally applicable under all conditions for these two latitude windows.

345



350 Figure 8: Measured  $[RO_2^*]$  vs  $\sqrt{P_{RO_2^*}}$  for the following latitudes: a) and c) south of 47°N; b) and d) north of 47°N. Note that a) and b) are colour-coded with  $j_{O(^1D)}$ ; c) and d) are colour-coded by  $NO_x$  mixing ratio. The dashed lines indicate the linear fit for visual support.

The relationship between  $RO_2^*$  and  $P_{RO_2^*}$  is further investigated to identify the dominant  $RO_2^*$  loss process in the air masses considered in this study. As stated in section 3,  $HO_2$  and  $RO_2$  are not speciated but retrieved as  $RO_2^*$  by the PerCEAS instrument. Because not all peroxy radicals are detected equally by the instrument, the comparison of measured and calculated  $RO_2^*$  values is complicated. To investigate this changes in the  $HO_2$  to the total  $RO_2^*$  ratios have been taken into consideration by  $\delta$ , i.e.,  $[HO_2] = \delta[RO_2^*]$  and  $[CH_3O_2] = (1 - \delta)[RO_2^*]$ , in the analysis. As a first approach,  $RO_2$  is assumed to consist only of  $CH_3O_2$  to reduce the complexity of the calculations by considering only  $CH_3O_2$  reaction rate constants. Moreover, in a previous study the ratio  $\alpha = eCL_{CH_3O_2}/eCL_{HO_2}$  was determined to be 65% for the measurement conditions (George et al., 2020).

360 The Eq. 5 is additionally extended to include  $RO_2^*$  effective yields from VOC oxidation and radical losses through HONO,  $HNO_3$ :

$$(2j_1[O_3]\beta + j_3[HONO])(1 - \rho) + 2j_8[HCHO] + 2j_9[CH_3CHO] + 2(j_{10a} + j_{10b})[CH_3C(O)CH_3] + 2j_{11}[CHOCHO] = \delta[RO_2^*](k_{23}[NO] + k_{24}[O_3])\rho + 2k_{15}\delta(1 - \delta)[RO_2^*]^2 + 2k_{16a}((1 - \delta)[RO_2^*])^2 + 2k_{14}(\delta[RO_2^*])^2 \quad (\text{Eq. 6})$$

where  $\beta$  is the effective yield of OH in the reaction of  $O(^1D)$  with  $H_2O$  given by:

$$\beta = \left( \frac{k_{2a}[H_2O]}{k_{2a}[H_2O] + k_{2b}[O_2] + k_{2c}[N_2]} \right),$$



365 On the left hand side of Eq. 6,  $1-\rho$  accounts for the effective yield of  $\text{HO}_2+\text{RO}_2$  through the radical initiation reactions R2a and R3 and reactions R5 to R7 and R12. As the calculation is constrained with on-board measurements, only the reactions of measured VOCs were considered in R12. Similarly,  $\rho$  accounts for the effective yield of HONO,  $\text{HNO}_3$  and  $\text{H}_2\text{O}$  formation through reactions R19 to R21 and the  $\text{HO}_2 + \text{NO}$  and  $\text{HO}_2 + \text{O}_3$  reactions (R23 and R24 respectively) on the right hand side of Eq. 6.

370 Consequently,  $\rho$  is given by:

$$\rho = \frac{(k_{19}[\text{NO}] + k_{20}[\text{NO}_2] + k_{21}[\text{HONO}])}{(k_5[\text{O}_3] + k_6[\text{CO}] + k_7[\text{CH}_4] + k_{12a}[\text{HCHO}] + k_{12b}[\text{CH}_3\text{CHO}] + k_{12c}[\text{CH}_3\text{C}(\text{O})\text{CH}_3] + k_{12d}[\text{CH}_3\text{OH}] + k_{12e}[\text{CHOCHO}] + k_{17}[\text{HO}_2] + k_{19}[\text{NO}] + k_{20}[\text{NO}_2] + k_{21}[\text{HONO}])}$$

375 Measurements of  $\text{CH}_4$ ,  $\text{HCHO}$ ,  $\text{CH}_3\text{CHO}$ ,  $\text{CHOCHO}$ ,  $\text{CH}_3\text{OH}$ , and  $\text{CH}_3\text{C}(\text{O})\text{CH}_3$  on-board HALO are available and implemented in Eq. 6. These comprise the most abundant and reactive OVOCs and are considered to be a representative surrogate for the VOCs that act as  $\text{RO}_2^*$  precursors through oxidation and photolysis. During the EMERGE campaign in Europe,  $k_{12a} \times \text{HCHO}$  and  $k_{12b} \times \text{CH}_3\text{CHO}$  have the highest contribution to the  $1 - \rho$  from all the OVOC measured. Their impact on the  $\text{RO}_2^*$  budget is found to be similar because their respective concentrations compensate the difference in the rate coefficients of their reactions with OH ( $k_{12a} =$   
380  $8.5 \times 10^{-12} \text{ cm}^3 \text{ molecule}^{-1} \text{ s}^{-1}$  and  $k_{12b} = 1.5 \times 10^{-11} \text{ cm}^3 \text{ molecule}^{-1} \text{ s}^{-1}$  at 298K and 1 atm.). Despite its high mixing ratios measured,  $\text{CH}_3\text{C}(\text{O})\text{CH}_3$  is less important in the  $1 - \rho$  term. This is because the rate coefficient  $k(T)_{12c}$  is significantly slower than  $k_{12a}$  and  $k_{12b}$  (see Table S1 in the supplement). Similarly, the contribution of  $\text{CHOCHO}$  and  $\text{CH}_3\text{OH}$  is an order of magnitude lower than that of  $\text{HCHO}$  and  $\text{CH}_3\text{CHO}$ .

Concerning the term  $\delta[\text{RO}_2^*](k_{23}[\text{NO}] + k_{24}[\text{O}_3])\rho$  on the right hand side of Eq.6, the  $\text{HO}_2$  reaction with  $\text{O}_3$  has a negligible  
385 effect as  $k_{24}$  is almost four orders of magnitude smaller than  $k_{23}$  and the  $\text{NO}$  concentrations remained about three orders of magnitude smaller than the  $\text{O}_3$  measured during the campaign.

The impact of the methylglyoxal ( $\text{CH}_3\text{C}(\text{O})\text{C}(\text{O})\text{H}$ ) photolysis was also investigated by using the  $\text{CH}_3\text{C}(\text{O})\text{C}(\text{O})\text{H}^*$  measurements provided by the miniDOAS instrument. The  $\text{CH}_3\text{C}(\text{O})\text{C}(\text{O})\text{H}^*$  measured is the sum of  $\text{CH}_3\text{C}(\text{O})\text{C}(\text{O})\text{H}$ , and a fraction of other substituted dicarbonyls (mainly 2,3-butanedione,  $\text{C}_3\text{H}_6\text{O}_2$ ), with similar visible absorption spectra. For the calculation,  
390  $\text{CH}_3\text{C}(\text{O})\text{C}(\text{O})\text{H}$  was assumed to be half of  $\text{CH}_3\text{C}(\text{O})\text{C}(\text{O})\text{H}^*$  as recommended by Zarzana et al. (2017) and Kluge et al. (2020). The  $\text{RO}_2^*$  calculated by including  $\text{CH}_3\text{C}(\text{O})\text{C}(\text{O})\text{H}$  photolysis systematically overestimated the measurements. As the adequacy of the recommended factor of 0.5 varies with the actual air mass composition,  $\text{CH}_3\text{C}(\text{O})\text{C}(\text{O})\text{H}$  was not included in the calculations.

Figure 9 shows the fractional contribution of the destruction rate ( $D_{\text{RO}_2^*}$ ) calculated for a 1:1 mixture of  $\text{HO}_2$  and  $\text{CH}_3\text{O}_2$  using the reactions included in Eq. 6 as a function of altitude. The data are classified into three groups according to the rate of destruction  
395 of  $\text{RO}_2^*$  mixing ratio  $D_{\text{RO}_2^*} < 0.01 \text{ pptv s}^{-1}$  (a),  $0.01 < D_{\text{RO}_2^*} < 0.9 \text{ pptv s}^{-1}$  (b), and  $D_{\text{RO}_2^*} > 0.9 \text{ pptv s}^{-1}$  (c) to show the lowest, most common, and highest ranges, respectively, encountered during the EMERGE campaign. For 90 % of the measurements,  $0.01 < D_{\text{RO}_2^*} < 0.9 \text{ pptv s}^{-1}$  applies, while the rest of the data are equally distributed in the other two  $D_{\text{RO}_2^*}$  ranges. The data in each group are always binned over 500 m when available.

As can be seen in Fig. 9, the  $\pm 1\sigma$  standard deviation of the obtained bins is very high. In spite of this, the  $\text{HO}_2 - \text{CH}_3\text{O}_2$  and  $\text{HO}_2 - \text{HO}_2$  reactions seem to dominate the radical destruction processes in the air masses probed. Their combined contribution is  $> 70\%$  in all the cases except in the 1000 m bin of  $D_{\text{RO}_2^*} > 0.9 \text{ pptv s}^{-1}$ . Other significant radical losses occur through the HONO and  $\text{HNO}_3$  formation. The contribution of the  $\text{CH}_3\text{O}_2 + \text{CH}_3\text{O}_2$  reaction to the total  $\text{RO}_2^*$  destruction rate is  $< 5\%$ .

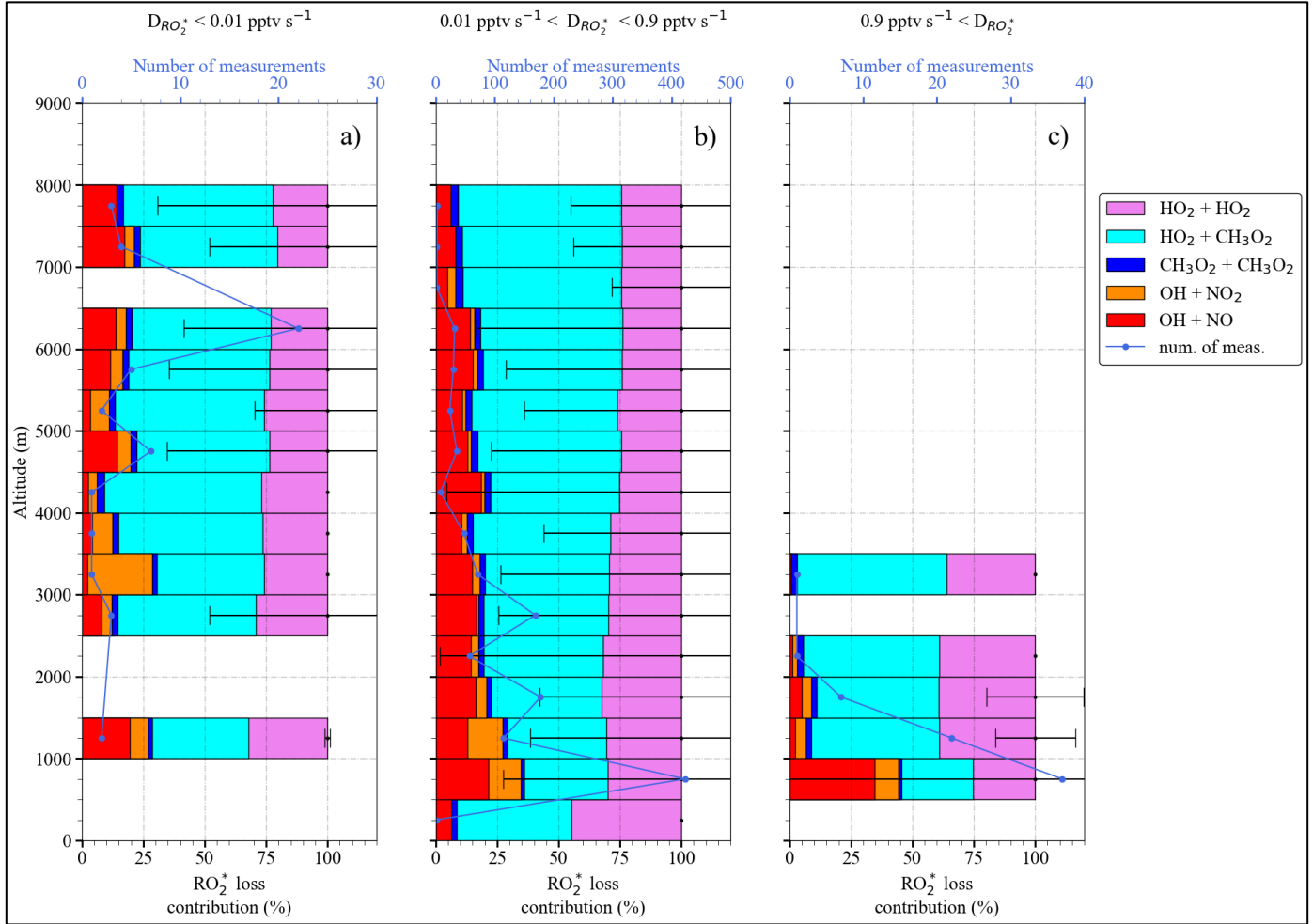


Figure 9:  $\text{RO}_2^*$  destruction rate  $D_{\text{RO}_2^*}$  and fractional contributions from loss reactions in Eq.6 as a function of altitude, for: a)  $D_{\text{RO}_2^*} < 0.01 \text{ pptv s}^{-1}$ , b)  $0.01 \text{ pptv s}^{-1} < D_{\text{RO}_2^*} < 0.9 \text{ pptv s}^{-1}$ , and c)  $D_{\text{RO}_2^*} > 0.9 \text{ pptv s}^{-1}$ . Note the different scales in the number of measurements.”

Since Eq. 6, is quadratic in  $[\text{RO}_2^*]$  it can be solved for  $[\text{RO}_2^*]_c$  where c stands for calculated, as:

$$[\text{RO}_2^*]_c = \frac{-(-L_{\text{RO}_2^*}) - \sqrt{L_{\text{RO}_2^*}^2 - 4(-2k_{\text{RO}_2^*})P_{\text{RO}_2^*}}}{2(-2k_{\text{RO}_2^*})} \quad (\text{Eq. 7})$$

where

$$k_{\text{RO}_2^*} = (k_{16a}(1 - \delta)^2 + k_{15}\delta(1 - \delta) + k_{14}\delta^2)$$

$$L_{\text{RO}_2^*} = (\delta(k_{23}[\text{NO}] + k_{24}[\text{O}_3])\rho)$$

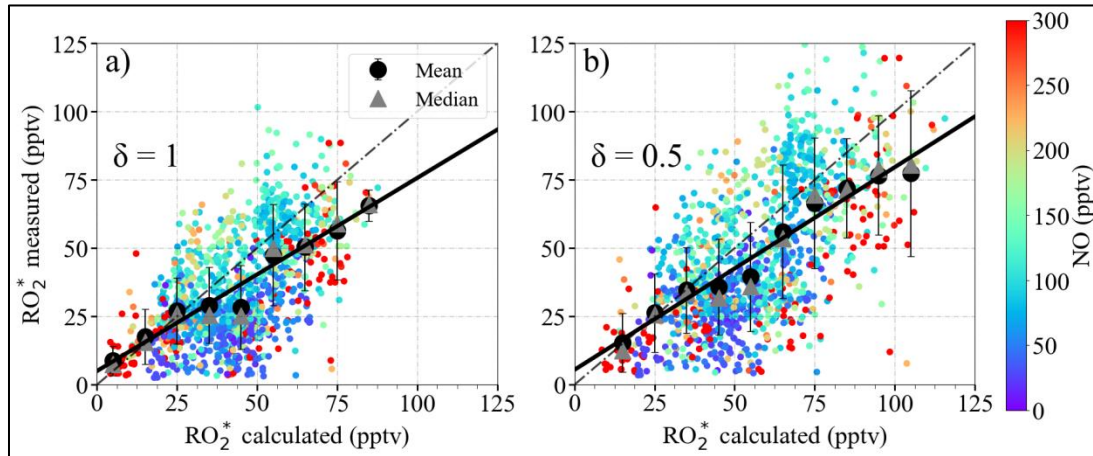
$$P_{\text{gRO}_2^*} = (2j_1[\text{O}_3]\beta + j_3[\text{HONO}])(1 - \rho) + 2j_8[\text{HCHO}] + 2j_9[\text{CH}_3\text{CHO}] + 2(j_{10a} + j_{10b})[\text{CH}_3\text{C}(\text{O})\text{CH}_3] + 2j_{11}[\text{CHOCHO}]$$

where  $k_{\text{RO}_2^*}$  is a weighed rate coefficient of  $\text{RO}_2^*$  self reactions for a 1:1 mixture of  $\text{HO}_2$  and  $\text{CH}_3\text{O}_2$ ,  $L_{\text{RO}_2^*}$  comprises the formation of HONO and  $\text{HNO}_3$  and  $P_{\text{gRO}_2^*}$  is the gross production of  $\text{RO}_2^*$ .

415 The second solution of the quadratic equation gives negative values for  $[RO_2^*]_c$ , therefore is assumed to have no physical meaning. A more detailed derivation of Eq. 6 and Eq. 7 are given in the supplementary information.

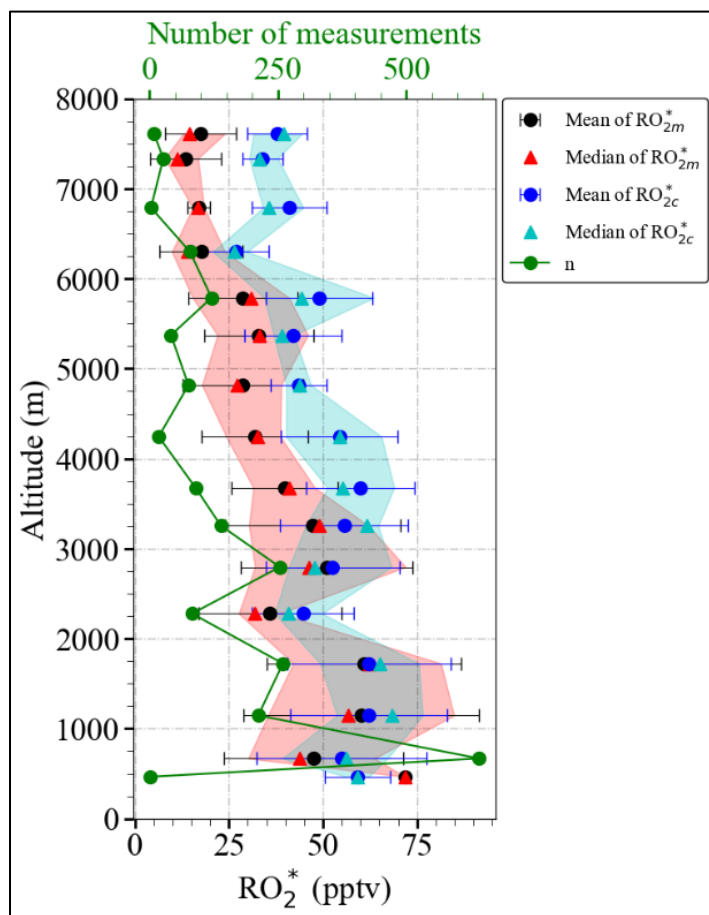
420 Figure 10 shows the measured  $RO_2^*$  (hereinafter referred to as  $RO_2^*_m$ ) mixing ratio versus the calculated  $RO_2^*_c$  mixing ratio using Eq. 7.  $RO_2^*_m$  and  $RO_2^*_c$  are the measured and calculated  $RO_2^*$  respectively for  $\delta = 1$ , i.e.  $RO_2^* = HO_2$  and  $\delta = 0.5$ , i.e.  $HO_2 = RO_2$ . The eCL corresponding to  $\delta = 1$  and  $\delta = 0.5$  used for the  $RO_2^*_m$  retrievals were determined in laboratory experiments, as reported by George et al. (2020). The small circles represent 1-minute  $RO_2^*_m$ , whereas the large circles are the mean of the  $RO_2^*_m$  binned over 10 pptv  $RO_2^*_c$  intervals. The  $RO_2^*$  data are colour-coded with the on-board NO measurements. The linear regression slopes are around 0.7 ( $R^2 = 0.96$ ), indicating an overall 25 – 30 % underestimation of the  $RO_2^*_m$ . The y-axis intercept is below the instrumental detection limit for most measurement conditions. Table 2: Linear regression parameters from  $RO_2^*_m$  versus  $RO_2^*_c$  using Eq. 7 from Fig.10.

Formula used to calculate $RO_2^*$	$\delta$	slope	y-intercept (pptv)	$R^2$
Eq. 7	1.00	0.71	5	0.96
	0.50	0.74	6	0.97



425 Figure 10:  $RO_2^*_m$  versus  $RO_2^*_c$  using Eq. 7 for a)  $\delta = 1$  and b)  $\delta = 0.5$ . The data are colour-coded with the measured NO mixing ratios. The 1-minute (small circles), the mean of the binned  $RO_2^*_m$  over 10 pptv  $RO_2^*_c$  intervals (large circles), and the median of each bin (grey triangles) are shown. The error bars indicate  $\pm 1\sigma$  standard deviation of each bin. The linear regression for the binned values (solid line) and the 1:1 relation (dashed line) are also depicted for reference.

430 Figure 11 shows the vertical profiles of  $RO_2^*_m$  and  $RO_2^*_c$  mixing ratios calculated for  $\delta = 0.5$ , averaged for the EMERGE flights over Europe in 500 m altitude bins.  $RO_2^*_c$  seems to overestimate  $RO_2^*_m$  for altitudes above 4000 m. As mentioned in Sect. 4.1, the vertical profiles are a composite from averaging flights with legs carried out at different longitude and latitudes. Therefore, the differences between  $RO_2^*_m$  and  $RO_2^*_c$  have been studied in more detail respect to the composition of the individual air masses (see the  $RO_2^*_m$  and  $RO_2^*_c$  mixing ratios as a function of latitude and altitude in Fig. S4 in the supplementary information).



435

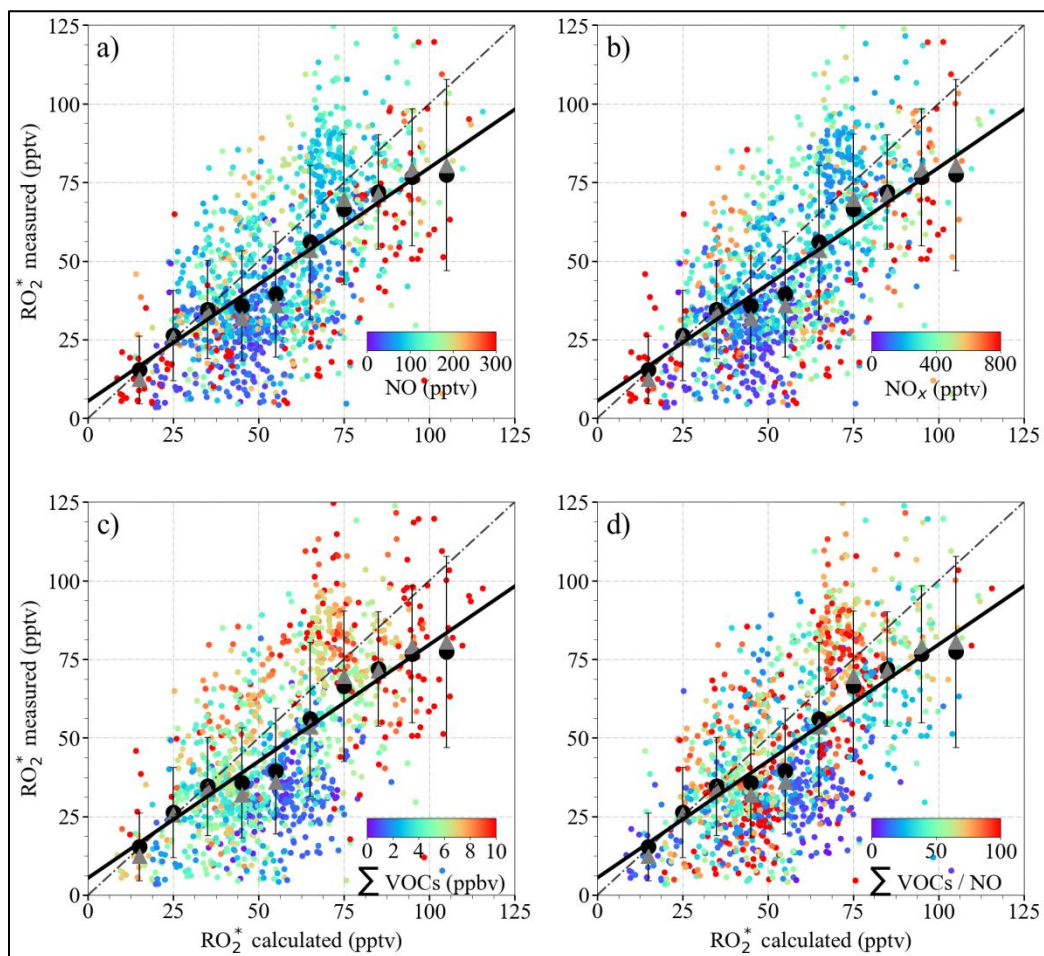
Figure 11: Vertical distribution of the mean  $RO_2^*{}_m$  and mean  $RO_2^*{}_c$  using Eq. 7 for  $\delta = 0.5$  for the EMERGe data set in Europe. The measurements are binned over 500 m altitude. The error bars are the  $\pm 1\sigma$  standard deviation of each bin. Median values (red and green triangles) the interquartile 25-75% range (red and blue shaded areas) and the number of individual measurements,  $n$ , for each bin (in green) are additionally plotted.

440

Figure 12 shows the data for  $\delta = 0.5$  colour-coded with NO,  $NO_x$ , the sum of HCHO, CH<sub>3</sub>CHO, CHOCHO, CH<sub>3</sub>OH, and CH<sub>3</sub>C(O)CH<sub>3</sub> (from now on referred to as  $\Sigma$ VOCs), as a surrogate for the amount of OVOCs acting as  $RO_2^*$  precursors, and the  $\Sigma$ VOCs to NO ratio. The largest differences between  $RO_2^*{}_m$  and  $RO_2^*{}_c$  are observed for the bins around 50 pptv. The  $RO_2^*{}_c$  overestimate the  $RO_2^*{}_m$  mostly for  $RO_2^*{}_m < 25$  pptv observed above  $\approx 4000$  m. These air masses are characterised by  $NO < 50$  pptv,  $\Sigma$ VOCs typically below 4 ppbv, high  $\Sigma$ VOCs/NO ratios ( $> 50$ ), and low insolation conditions, i.e.  $j_{O(^1D)} < 2 \times 10^{-5} s^{-1}$  (see Fig. S5 in the supplementary information). Under these insolation conditions, the radical production rate is expected to be low, and the  $RO_2^* - RO_2^*$  reactions are expected to dominate the  $RO_2^*$  loss processes. As OH and H<sub>2</sub>O<sub>2</sub> were not measured during the EMERGe campaign in Europe, Eq. 7 does not include the loss reactions R17 and R18, which might be significant under such conditions (Tan et al., 2001) and explain the overestimation of  $RO_2^*{}_m$ . This is also the case for the overestimations observed below 40 pptv  $RO_2^*{}_m$  at other altitudes, where  $NO < 50$  pptv but the  $\Sigma$ VOCs/NO ratios remain low. The overestimation may therefore be independent of the  $\Sigma$ VOCs/NO ratios. For  $NO \leq 50$  pptv,  $NO_2 \leq 100$  pptv,  $RO_2^* \leq 40$  pptv and  $HCHO \leq 1$  ppbv, the rate of reaction R17, which forms H<sub>2</sub>O and O<sub>2</sub> from OH and HO<sub>2</sub>, is about 4 times faster than the rate of the OH oxidation reaction of the dominant OVOCs (R12) considered in this study or the rate of formation of HONO (R19).

450

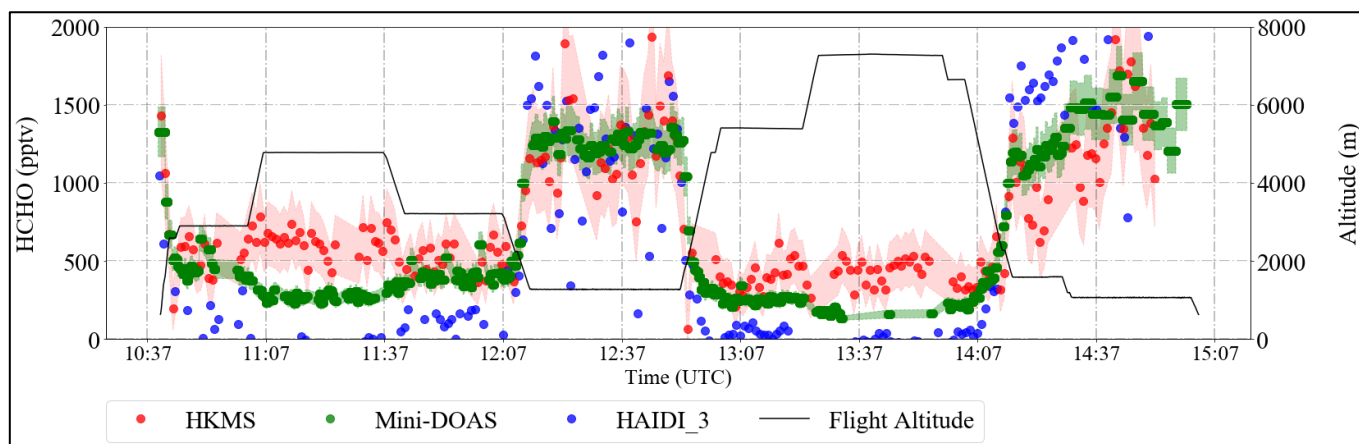
455  $RO_2^*{}_m$  is both underestimated and overestimated for  $\Sigma VOCs$  mixing ratios greater than 7 ppbv. The composition of these air masses is very different, as reflected by the  $\Sigma VOCs/NO$  ratios. This implies that Eq. 7 does not capture the peroxy radical yields adequately from the measured VOCs and OVOC in these cases. The differences between  $RO_2^*{}_m$  and  $RO_2^*{}_c$  may be explained in part by a) changes in OH yields due to additional VOC oxidation processes, which are not in Eq. 7 and/or b)  $RO_2^*$  production from the photolysis of carbonyls, which were not measured and/or c)  $RO_2^*$  production from the ozonolysis of alkenes or unidentified biogenic terpene emissions and/or d) overestimation of the loss processes. For  $VOC < 2ppb$  and  $\Sigma VOCs/NO < 20$ ,  $RO_2^*{}_m$  is 460 systematically overestimated. This might indicate underestimation in the radical losses through nitrite and nitrate formation.



465 Figure 12:  $RO_2^*{}_m$  versus  $RO_2^*{}_c$  using Eq. 7 for  $\delta = 0.5$  colour-coded with the measured a) NO mixing ratio, b)  $NO_x$  mixing ratio, c)  $\Sigma VOCs$  mixing ratio, where  $\Sigma VOCs = HCHO + CH_3CHO + (CHO)_2 + CH_3OH + CH_3C(O)CH_3$ , and d)  $\Sigma VOCs/NO$  ratio. The 1-minute (small circles), the mean of the binned  $RO_2^*{}_m$  over 10 pptv  $RO_2^*{}_c$  intervals (large circles), and the median of each bin (triangles) are shown. The error bars represent the  $\pm 1\sigma$  standard deviation of each bin. The linear regression for the binned values (solid line) and the 1:1 relationship (dashed line) are plotted for reference.

Although considered small, the spatial and temporal differences in the in-situ measurements of the key trace gases ( $O_3$ , NO,  $H_2O$ , CO,  $CH_4$ , VOCs) as compared to those of the remote sensing observations ( $NO_2$  and HONO) used in Eq. 7 may also contribute to the overall spread observed in Fig. 12. Although the temporal evolution and the amount of the trace gases measured using in-situ and remote sensing instruments agree reasonably well, as shown for HCHO in Fig. 13, the remote sensing instruments have, in general, larger air sampling volumes compared to that of in-situ instruments. This may occasionally lead to significant differences 470 depending on the location of the pollutant layers with respect to HALO. In addition, PTR-MS measurements of HCHO might

include interferences from molecular fragments of other compounds in the sample air (Inomata et al., 2008). Further details about the accuracy and comparability of the instrumentation on-board during the campaign can be found elsewhere (Schumann, 2020).



475

Figure 13: An example of the time series of the measured HCHO mixing ratios retrieved from the remote sensing (HAIDI in blue and miniDOAS in green) and in-situ (HKMS in red) instruments during the E-EU-04 flight on 14.07.2017. The shaded region shows  $\pm 1\sigma$  uncertainties of the HKMS and miniDOAS instruments. The flight altitude is depicted in black.

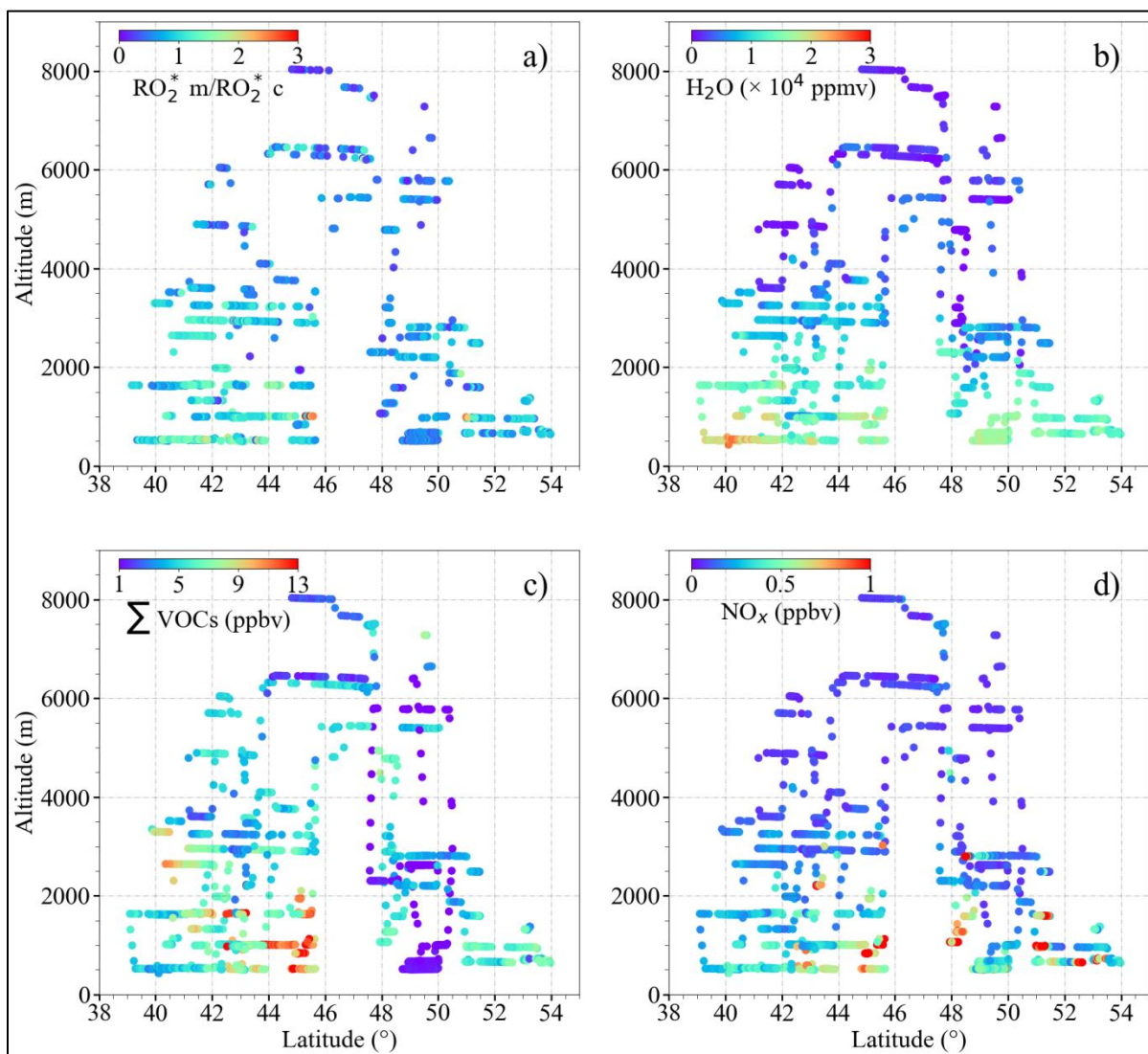
480

In summary, apart from the inaccuracies in the reaction rate coefficients, the differences between  $RO_2^*_m$  and  $RO_2^*_c$  might be caused by a combined effect of the limitations of the analytical expression to simulate complex non-linear chemistry and the measurement uncertainties arising from the spatial heterogeneity of the plume for the remote sensing instruments. Consequently, the quantification of limiting factors in Eq. 7 require the analysis of the pollution events encountered along the flights individually.

485

The ratio of  $RO_2^*_m$  to  $RO_2^*_c$  ( $RO_2^*_m/RO_2^*_c$ ) has been used to assess the applicability of Eq. 7 for the calculation of  $RO_2^*$  in the air masses probed. In Fig. 14, the data are colour-coded with respect to  $RO_2^*_m/RO_2^*_c$ ,  $H_2O$ ,  $\Sigma VOCs$ , and  $NO_x$ . The air masses probed at altitudes above 2000 m are close to the PSS assumptions used to develop Eq. 7, and consequently, the  $RO_2^*_m/RO_2^*_c$  remains  $\leq 1$ . In contrast,  $RO_2^*_m/RO_2^*_c$  is at its highest value below 2000 m, reaching up to 3. At these altitudes, most of the flights in Europe were carried out in pollution plumes, in which both the amount of  $NO_x$  and  $RO_2^*$  precursors are high. The analytical expression does not capture the  $RO_2^*$  variations resulting from fast non-linear photochemistry present in these pollution plumes. This is the case for the measurements made between  $42^\circ N$  and  $46^\circ N$  in the outflow of Po Valley and Rome.  $\Sigma VOCs > 7$  ppbv and  $NO_x$  mixing ratios  $> 500$  pptv indicate high radical precursor loading and relatively fresh emissions. The  $RO_2^*_m/RO_2^*_c$  is also  $> 2$  in the measurements over the English Channel (between  $50^\circ N$  and  $52^\circ N$ ) with  $\Sigma VOCs$  and  $NO_x$  mixing ratio  $> 7$  ppbv and 1000 pptv, respectively.

490

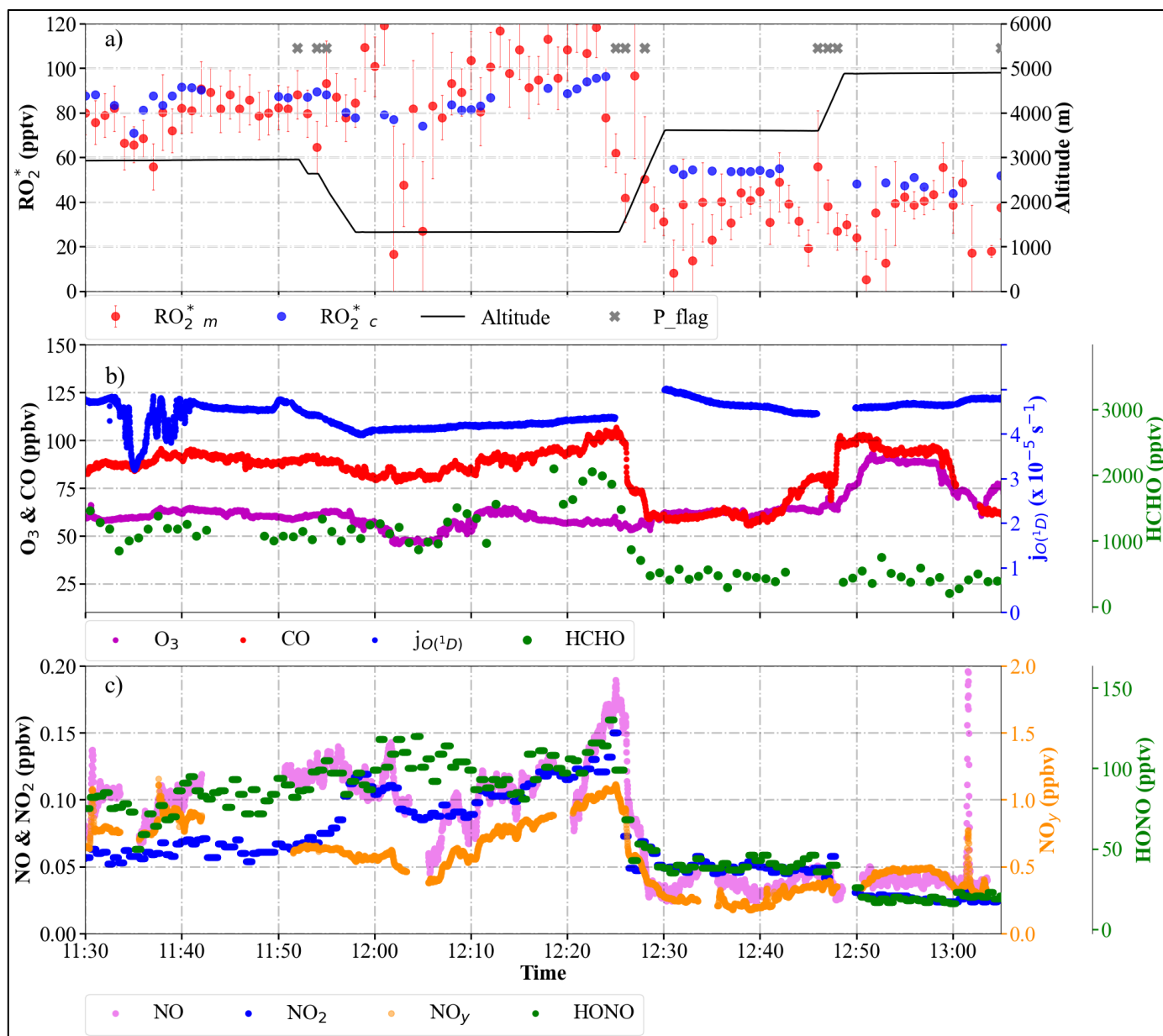


495 Figure 14: Plots of a) the ratio of  $RO_2^*_m$  to  $RO_2^*_c$  ( $RO_2^*_m/RO_2^*_c$ ) assuming that  $\delta = 0.5$ ; b)  $H_2O$ ; c)  $\sum VOCs$ ; d)  $NO_x$  as a function of latitude and altitude for the EMeRGe measurements in Europe.

The applicability of Eq. 7 for calculating the in-flight measurements of  $RO_2^*$  along the track of the E-EU-03 flight on 11 July 2017 was studied in more detail. The E-EU-03 flight investigated the outflow of selected MPCs in Italy (i.e., Po Valley and Rome). Consequently, the flight track was routed along the western coast of Italy and included vertical profiling over the Tyrrhenian Sea upwind of Rome (see Fig. S6 in the supplementary information). As indicated by  $j_{O(^1D)}$ , in Fig. 15, cloudless conditions dominated throughout the flight track. The  $RO_2^*_c$  agree reasonably well with  $RO_2^*_m$  throughout this period except in the pollution plume measured from 12:05 to 12:25 UTC. In this plume, CO, NO,  $NO_2$ , HONO,  $NO_y$ , and HCHO were 100 ppbv, 180 pptv, 150 pptv, 120 pptv, 1ppbv and 2 ppbv, respectively. The  $RO_2^*_m$  are approximately 20 % underestimated by  $RO_2^*_c$  during this period. Backward trajectories calculated using FLEXTRA indicate the transport of pollution through the Mediterranean mixed with dust plumes originating from Tunisia. The NO mixing ratios observed indicate the proximity to emission sources.

505 The measurements of VOCs used in Eq. 7 may not be representative of the actual complex VOC composition in the plume measured from 12:05 to 12:25 UTC. Consequently, the  $RO_2$  to  $HO_2$  ratio, the branching ratios and effective rate coefficients for  $RO_2^* - RO_2^*$  reactions might not be well represented in Eq. 7. Taking  $CH_3O_2$  as a surrogate for all  $RO_2$  might lead to uncertainties

in the  $RO_2^*$  calculations in the presence of OVOCs with larger organic chains. On the experimental side, changes in the  $HO_2$  to  $RO_2$  ratio affect the accuracy of the PerCEAS retrieval of the total sum of radicals. As noted in section 3, in this study  $RO_2^* = HO_2 + 0.65 \times RO_2$ , and the eCL is determined for a 1:1 mixture of  $HO_2:CH_3O_2$ , i.e.  $\delta = 0.5$  is used for the  $RO_2^*$  retrieval. However, the  $HO_2$  to  $CH_3O_2$  ratio is not expected to remain constant in all the air masses probed. For a 3:1 ratio of  $HO_2:RO_2$ , the  $RO_2^*_m$  would decrease by 10 %. Similarly, a  $HO_2:RO_2$  ratio of 1:3 would lead to an increase of 10 % in the reported  $RO_2^*_m$ . This uncertainty is well below the in-flight uncertainty of the PerCEAS instrument indicated by the error bars in Fig. 14 (George et al., 2020), and cannot account for the overall underestimation. However, it might reduce the differences observed between  $RO_2^*_m$  and  $RO_2^*_c$  in particular cases. A complete explanation of the variability of  $RO_2^*$  in the pollution plumes measured within the campaign in Europe is beyond the scope of this analysis and requires an investigation by high-resolution chemical models.



520 Figure 15: Temporal variation of  $RO_2^*_m$  and  $RO_2^*_c$ , selected radical precursors and  $j_{O(^1D)}$  along the E-EU-03 flight track: a)  $RO_2^*_m$ ,  $RO_2^*_c$  mixing ratios. The flight altitude is indicated in black. The P\_flag indicates  $RO_2^*$  measurements affected by dynamical pressure variation in the inlet; b)  $O_3$ , CO, HCHO mixing ratios, and  $j_{O(^1D)}$ ; c) NO, NO<sub>2</sub>, NO<sub>y</sub>, and HONO mixing ratios.



#### 4.4. Comparison of results with other studies

##### 4.4.1 RO<sub>2</sub><sup>\*</sup> production rate

525 Cantrell et al. (2003b) proposed that the production of RO<sub>2</sub><sup>\*</sup>, P<sub>RO<sub>2</sub><sup>\*</sup></sub>, is equal to the sum of two terms representing RO<sub>2</sub><sup>\*</sup> – RO<sub>2</sub><sup>\*</sup> reactions and the RO<sub>2</sub><sup>\*</sup> – NO<sub>x</sub> reactions in the troposphere. As a result of this assumption, these authors describe the relationship between HO<sub>2</sub>, RO<sub>2</sub>, P<sub>RO<sub>2</sub><sup>\*</sup></sub> and NO<sub>x</sub> as:

$$P_{RO_2^*} = k_{RR} [HO_2 + RO_2]^2 + k_{RN} [HO_2 + RO_2] [NO_x] \quad (\text{Eq. 9})$$

where k<sub>RR</sub> and k<sub>RN</sub> refer to effective rate coefficients for RO<sub>2</sub><sup>\*</sup> – RO<sub>2</sub><sup>\*</sup> and RO<sub>2</sub><sup>\*</sup> – NO<sub>x</sub> reactions, and are calculated as fit parameters.

530 Solving Eq. 9 for [HO<sub>2</sub> + RO<sub>2</sub>]<sup>2</sup> leads to:

$$[HO_2 + RO_2] = \sqrt[2]{A + B^2} - B \quad (\text{Eq. 10})$$

where  $A = \frac{P_{RO_2^*}}{k_{RR}}$  and  $B = \frac{k_{RN}[NO_x]}{2 k_{RR}}$ . For low NO<sub>x</sub> and/or high P<sub>RO<sub>2</sub><sup>\*</sup></sub>, B becomes negligible compared to A. Then [HO<sub>2</sub> + RO<sub>2</sub>] approaches  $\sqrt[2]{A}$  and is independent of NO<sub>x</sub>. For high NO<sub>x</sub> and /or low P<sub>RO<sub>2</sub><sup>\*</sup></sub>, [HO<sub>2</sub> + RO<sub>2</sub>] approaches zero.

535 The RO<sub>2</sub><sup>\*</sup><sub>m</sub> and RO<sub>2</sub><sup>\*</sup><sub>c</sub> for the EMERGe observations in Europe, binned in 0.1 pptv s<sup>-1</sup> P<sub>RO<sub>2</sub><sup>\*</sup></sub> intervals, were fitted according to the procedure of Cantrell et al. (2003b) and the results are shown in Fig. 16. The obtained fit parameters for Fig. 16a and Fig. 16b are k<sub>RR</sub> = 7 × 10<sup>-5</sup>; k<sub>RN</sub> = 9 × 10<sup>-6</sup>. The RO<sub>2</sub><sup>\*</sup> calculated by Eq. 7 appears to be close to the linear function of the NO<sub>x</sub> measured. Similar to the results of the study of Cantrell et al. (2003b), a decrease of RO<sub>2</sub><sup>\*</sup> with NO<sub>x</sub> is identified for NO<sub>x</sub> > 1000 pptv, although only for P<sub>RO<sub>2</sub><sup>\*</sup></sub> < 0.7 pptv s<sup>-1</sup>. In the study of Cantrell et al. (2003b), P<sub>RO<sub>2</sub><sup>\*</sup></sub> only reached values up to 0.275 pptv s<sup>-1</sup>.

540 Despite the low agreement of the fitted lines with the RO<sub>2</sub><sup>\*</sup><sub>m</sub>, a decrease of the RO<sub>2</sub><sup>\*</sup><sub>m</sub> as a function of NO<sub>x</sub> is still observed. The disagreement between the RO<sub>2</sub><sup>\*</sup><sub>m</sub> and the curves estimated using Eq. 10 implies that the simplified Eq. 9 from Cantrell et al. (2003b), is insufficient to adequately describe the chemical and physical processes occurring in the air masses probed. Part of the disagreement might arise from missing terms in the P<sub>RO<sub>2</sub><sup>\*</sup></sub> calculation or inaccuracies related to the NO to NO<sub>2</sub> ratio in the air mass, which are more evident at higher P<sub>RO<sub>2</sub><sup>\*</sup></sub>. As expected, the ratio of calculated [RO<sub>2</sub><sup>\*</sup><sub>c</sub>] to  $\sqrt[2]{P_{RO_2^*}}$  has a negative linear dependence on the measured [NO<sub>x</sub>] (see Fig. 16c). The comparable relationship of [RO<sub>2</sub><sup>\*</sup><sub>m</sub>] /  $\sqrt[2]{P_{RO_2^*}}$  to [NO<sub>x</sub>] is not linear for NO<sub>x</sub> < 100 pptv approximately (see Fig. 16d). This indicates that the simplified approach of Cantrell et al. (2003b) is not applicable to the more  
545 complex non-linear processes involved in the air masses investigated within EMERGe.

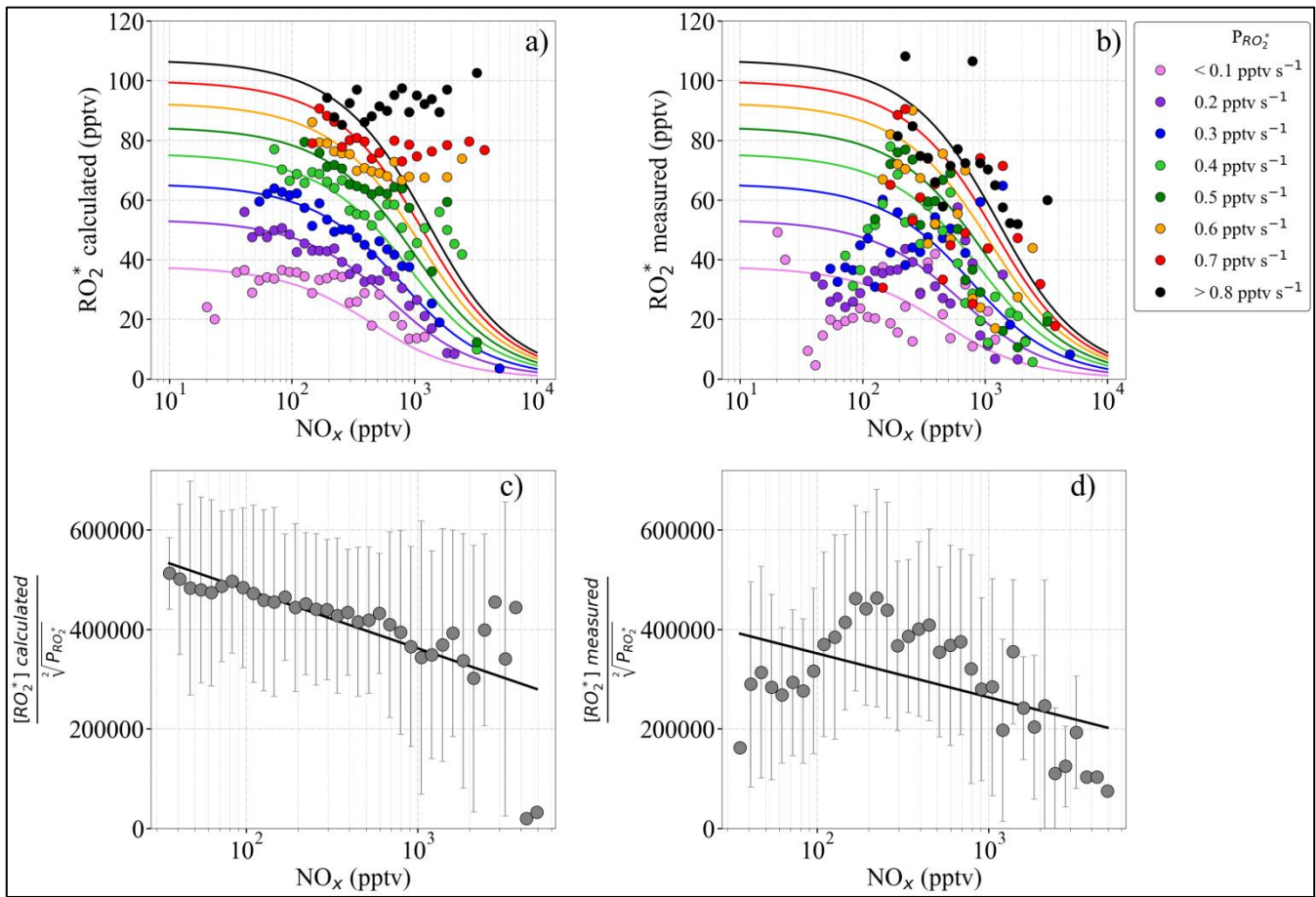


Figure 16: a)  $RO_2^*{}_c$  binned into  $P_{RO_2^*}$  intervals of  $0.1 \text{ pptv s}^{-1}$  versus binned  $NO_x$ ; b)  $RO_2^*{}_m$  binned into  $P_{RO_2^*}$  intervals of  $0.1 \text{ pptv s}^{-1}$  versus binned  $NO_x$ ; c) ratio of  $[RO_2^*]_c$  to  $\sqrt{P_{RO_2^*}}$  versus  $NO_x$ ; and d)  $[RO_2^*]_m$  to  $\sqrt{P_{RO_2^*}}$  ratio versus  $NO_x$ . The data in the a) and b) panels are assigned different colours, as a function of the radical production rate interval. The  $NO_x$  observations are binned into 50 equidistant intervals on a logarithmic scale. The solid lines in panels a) and b) are the least square fits, obtained using Eq. 9. In panels c) and d) the ratio of  $[RO_2^*]_c$  to  $\sqrt{P_{RO_2^*}}$  and  $[RO_2^*]_m$  to  $\sqrt{P_{RO_2^*}}$  are binned into 50  $NO_x$  intervals equidistant on the logarithmic scale from 10 to 10000 pptv. Error bars indicate the  $\pm 1\sigma$  standard deviation for the distribution in each bin.

#### 4.4.2 $O_3$ production rate

The  $O_3$  production rate ( $P_{O_3}$ ) is calculated from the EMERGE Europe dataset using the reaction of  $RO_2^*$  with NO in a similar manner to that used in previous studies of photochemical processes in urban environments (e.g. Kleinman et al., 1995; Volz-Thomas et al., 2003; Mihelcic et al., 2003; Cantrell et al., 2003b; and references herein).

$$P_{O_3} = k_{RO_2^*+NO}[RO_2^*][NO] \quad (\text{Eq. 11})$$

where  $k_{RO_2^*+NO}$  is taken as the average of  $k_{HO_2+NO}$  and  $k_{CH_3O_2+NO}$ .

Figure 17 shows the mean  $P_{O_3}$  calculated using Eq. 11 from the  $RO_2^*{}_m$  and  $RO_2^*{}_c$  as a function of NO. The measurements are binned into 50 NO mixing ratio bins. The bin size increases with NO to keep the points equidistant on the logarithmic scale. The calculated  $P_{O_3}$  for the  $RO_2^*{}_m$  and  $RO_2^*{}_c$  agree well within the standard deviation of the bins.

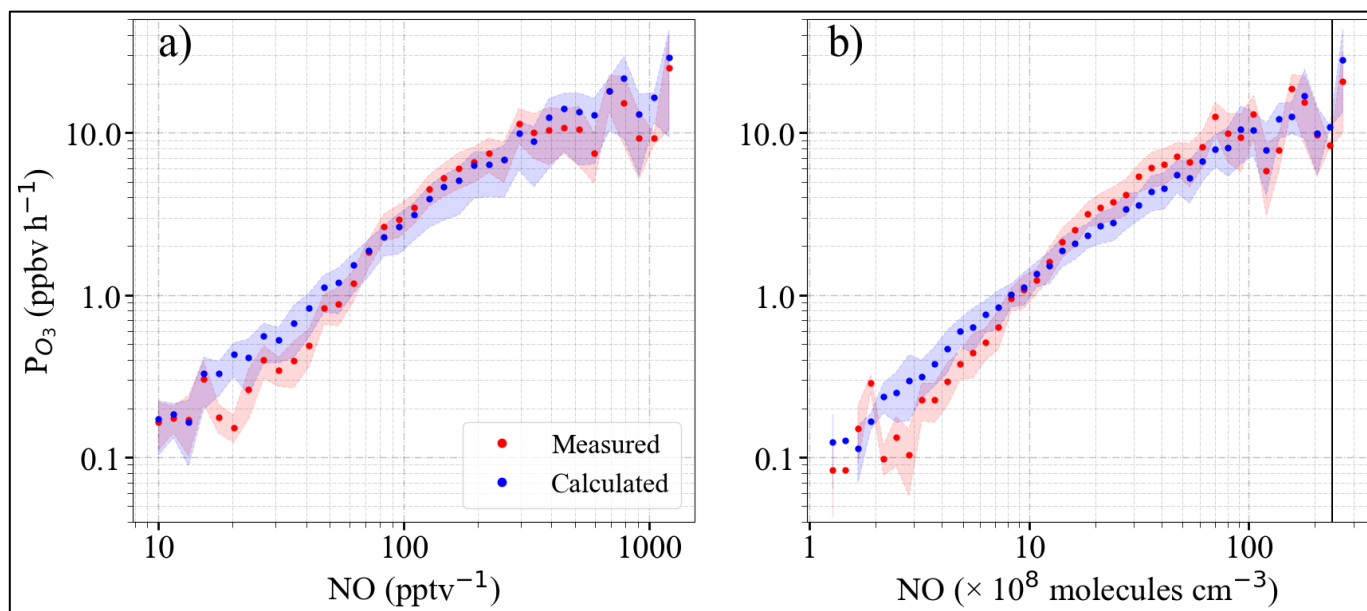


Figure 17: Calculated  $O_3$  production rate ( $P_{O_3}$ ) determined using  $RO_2^*{}_m$  (red dots) and  $RO_2^*{}_c$  (blue dots) as a function of: a) NO mixing ratio; b) NO number density. The 1-minute measurements are binned into 50 bins of NO equidistant on the logarithmic scale for panel a) from 10 to 10000 pptv and for panel b) from  $5 \times 10^7$  to  $3.5 \times 10^{10}$  molecules  $cm^{-3}$  respectively. The shaded area shows the  $\pm 1\sigma$  standard deviation of each bin. To facilitate comparison with ground-based measurements, the black line plotted in panel b) is the number density corresponding to 1 ppbv NO at 1000 mbar and 25°C.

Similar  $P_{O_3}$  values have been reported for ground-based measurements in polluted areas such as Wangdu (Tan et al., 2017) and Beijing (Whalley et al., 2021) and similar ranges of peroxy radicals and NO mixing ratios. In previous work, Whalley et al. (2018) calculated  $P_{O_3}$  to be about an order of magnitude lower than that found in this study from observations in central London for about an order of magnitude lower amount of  $HO_2 + RO_2$ . For  $NO > 1$  ppbv, the  $P_{O_3}$  estimated from the measurement of  $HO_2$  and  $RO_2$ , or from the assumptions of an  $HO_2$  to  $RO_2$  ratio were underestimated by the models in other studies in the urban atmosphere (e.g. Martinez et al., 2003; Ren et al., 2003; Kanaya et al., 2008; Mao et al., 2010; Kanaya et al., 2012; Ren et al., 2013; Brune et al., 2016; Griffith et al., 2016). This behaviour is generally attributed to an underestimate of large  $RO_2$  concentrations, which likely undergo multiple bimolecular reactions with NO before forming an  $HO_2$  radical.

During the EMERGE campaign in Europe, the NO mixing ratios were  $< 1$  ppbv (approximately  $< 3 \times 10^{10}$  molecules  $cm^{-3}$ ). The ozone production rates obtained for both  $RO_2^*{}_m$  and  $RO_2^*{}_c$  are in reasonable agreement with other modelling studies in urban environments where the mixing ratio of NO is  $< 1$  ppbv (Tan et al., 2017; Whalley et al., 2021)

## 5. Summary and conclusions

This study exploits the airborne measurements of various atmospheric constituents on-board the HALO research aircraft over Europe in summer 2017 to investigate radical photochemistry in the probed airmasses.  $RO_2^*$  are calculated by assuming a photostationary steady-state (PSS) of  $RO_2^*$  and compared with the actual measurements. The calculation is constrained by the simultaneous airborne measurements of radical precursors, photolysis frequencies and reactants of  $RO_2^*$  such as  $NO_x$  and  $O_3$ . The calculated radical production rates  $P_{RO_2^*}$  do not significantly vary with altitude in the air masses investigated as the increase in the photolysis frequencies as a function of altitude is concurrent with decreases in precursor concentrations.

The significance and the importance of selected initiating and terminating processes in the  $\text{RO}_2^*$  chemistry are investigated by gradually increasing the complexity of the analytical expression. The agreement of the calculations with the measurements over a wide range of chemical composition and insolation conditions improves when the analytical expression is extended to account for effective radical yields from VOC oxidation and radical losses through nitrates and nitrites formation. The  $\text{RO}_2^*$  measured is usually overestimated when  $\text{NO}$  is  $< 50$  pptv in the air probed. This behavior might be explained by  $\text{RO}_2^*$  loss processes involving reactions with OH (e.g. the reaction of  $\text{HO}_2$  with OH, but possibly to a lesser extent the three body reaction of OH with itself to make  $\text{H}_2\text{O}_2$ ). These reactions may become significant  $\text{RO}_2^*$  loss processes at low  $\text{NO}$  concentrations as measured during the campaign but are excluded from the analytical expression, which is constrained by on-board measurements..

The  $\text{RO}_2^*$  calculated under assumption of a photostationary state mostly underestimated the  $\text{RO}_2^*$  measured in polluted plumes of urban origin at altitudes below 2000 m. Changes in the  $\text{HO}_2$  to  $\text{RO}_2$  ratios in different plumes can account for the disagreement in particular cases. In pollution plumes with the sum of the OVOCs measured mixing ratios being higher than 7 ppbv approximately, the underestimation of the measurements can reach up to 80 %. In these plumes, the oxidation and/or photolysis of VOCs, which were not measured, and the ozonolysis of alkenes might be significant sources of  $\text{RO}_2^*$ , limiting the accuracy of the analytical expression.. More information about peroxy radical speciation and VOC partitioning is required to better describe the fast photochemistry in these pollution plumes.

However, the analytical expression developed is robust enough to simulate the radical chemistry in most of the conditions in the free troposphere encountered during EMeRGe in Europe. Speciated radical and VOC measurements in future campaigns would facilitate the estimation of radical loss reactions in air masses having  $\text{NO} < 50$  pptv and improve radical production rates estimations in pollution plumes having a high amount of VOCs, where non-linear complex chemistry is involved. Comparing  $\text{RO}_2^*$  measurements with  $\text{RO}_2^*$  calculations from the analytical expression helps to identify different chemical and physical regimes, which can be used to constrain future model studies.

The calculated  $\text{O}_3$  production rates for  $\text{NO} < 1$  ppbv are in the same order of magnitude as those previously reported for urban environments. This indicates that the selected  $\text{RO}_2^*$  production and loss processes and observations of the radical precursors on-board are, to a good approximation, adequate for the estimation of the  $\text{O}_3$  production in the measured airmasses in the free troposphere over Europe.

*Disclaimer. Competing interests.* The authors declare that they have no conflict of interest.

*Disclaimer. Financial support.* The study was funded in part by the German Research Foundation (Deutsche Forschungsgemeinschaft; DFG) HALO-SPP 1294, the University and the State of Bremen, IPA, DLR, Oberpfaffenhofen, Germany. The contributions from BS, FK, and KP were supported via the DFG grants PF 384/16, PF 384/17 and PF 384/19. KB was granted funding via the DFG grant PI 193/21-1 and acknowledges additional financial from the Heidelberg Graduate School for Physics. EF was supported via the DFG grant NE 2150/1-1 and acknowledges additional financial support from the Karlsruhe Institute of Technology. MG, YL, MDAH and JPB acknowledge financial support from the University of Bremen.

## 620 Acknowledgements

### Author contribution:

MG, VN, and YL undertook the  $\text{RO}_2^*$  measurements, flying as key scientists on-board HALO. VN led the deployment of PeRCEAS in the HALO aircraft. MG led the analysis of the PeRCEAS measurements and prepared the manuscript with contributions from all co-authors. MDAH and JPB initiated the EMeRGe research project and consortium, acted as co-principal and principal

625 investigators, and participated in the measurement campaigns. They developed the overarching EMERGe scientific objectives and the required measurement portfolio, directed the EMERGe research campaigns, and participated in the data analysis presented. AZ, BB, BS, EF, FO, FK, HS, HZ, KB, KP, and TH have contributed by providing their measurements made on-board HALO during the campaign and participated in the discussion of results.

#### Competing interests:

630 The authors declare that they have no conflict of interest.

## 6. References

Andreae, M. O. , Afchine, A. Albrecht, R., Holanda, B. A., Artaxo, P., Barbosa, H. M. J., Borrmann, S., Cecchini, M. A., Costa, A., Dollner, M., Fütterer, D., Järvinen, E., Jurkat, T., Klimach, T., Konemann, T., Knote, C., Krämer, M., Krisna, T., Machado, L. A. T., Mertes, S.; Minikin, A. , Pöhlker, C., Pöhlker, M. L., Pöschl, U. Rosenfeld, D., Sauer, D., Schlager, H., Schnaiter, M.,  
635 Schneider, J., Schulz, C., Spanu, A., Sperling, V. B., Voigt, C., Walser, A., Wang, J., Weinzierl, B., Wendisch, M. , Ziereis, H.: Aerosol characteristics and particle production in the upper troposphere over the Amazon Basin. *Atmos. Chem. Phys.*, 18, 921–961, <https://doi.org/10.5194/acp-18-921-2018>, 2018.

Andrés-Hernández, M. D., Kartal, D., Reichert, L., Burrows, J. P., Meyer Arnek, J., Lichtenstern, M., Stock, P., and Schlager, H.: Peroxy radical observations over West Africa during AMMA 2006: photochemical activity in the outflow of convective systems,  
640 *Atmos. Chem. Phys.*, 9, 3681–3695, <https://doi.org/10.5194/acp-9-3681-2009>, 2009.

Andrés Hernández, M. D., Hilboll, A., Ziereis, H., Förster, E., Krüger, O. O., Kaiser, K., Schneider, J., Barnaba, F., Vrekoussis, M., Schmidt, J., Huntrieser, H., Blechschmidt, A.-M., George, M., Nenakhov, V., Klausner, T., Holanda, B. A., Wolf, J., Eirenschmalz, L., Krebsbach, M., Pöhlker, M. L., Hedegaard, A. B., Mei, L., Pfeilsticker, K., Liu, Y., Koppmann, R., Schlager, H., Bohn, B., Schumann, U., Richter, A., Schreiner, B., Sauer, D., Baumann, R., Mertens, M., Jöckel, P., Kilian, M., Stratmann, G., Pöhlker, C., Campanelli, M., Pandolfi, M., Sicard, M., Gomez-Amo, J. L., Pujadas, M., Bigge, K., Kluge, F., Schwarz, A.,  
645 Daskalakis, N., Walter, D., Zahn, A., Pöschl, U., Bönisch, H., Borrmann, S., Platt, U., and Burrows, J. P.: Overview: On the transport and transformation of pollutants in the outflow of major population centres – observational data from the EMERGe European intensive operational period in summer 2017, *Atmos. Chem. Phys.*, 22, 5877–5924, 2022  
<https://doi.org/10.5194/acp-22-5877-2022>, 2022 Brito, J., and Zahn, A.: An unheated permeation device for calibrating  
650 atmospheric VOC measurements, *Atmos. Meas. Tech.*, 4(10), 2143–2152, <https://doi.org/10.5194/amt-4-2143-2011>, 2011.

Brune, W. H., Baier, B. C., Thomas, J., Ren, X., Cohen, R. C., Pusede, S. E., Browne, E. C., Goldstein, A. H., Gentner, D. R., Keutsch, F. N., Thornton, J. A., Harrold, S., Lopez-Hilfiker, F. D., and Wennberg, P. O.: Ozone production chemistry in the presence of urban plumes, *Faraday Discuss.*, 189, 169–189, <https://doi.org/10.1039/c5fd00204d>, 2016.

Burkholder, J. B., Sander, S. P., Abbatt, J., Barker, J. R., Huie, R. E., Kolb, C. E., Kurylo, M. J., Orkin, V. L. Wilmouth, D. M.,  
655 and Wine P. H.: Chemical Kinetics and Photochemical Data for Use in Atmospheric Studies, Evaluation No. 18, JPL Publication 15-10, Jet Propulsion Laboratory, Pasadena, available at: <http://jpldataeval.jpl.nasa.gov> (last access: 7 April 2020), 2015.

- Cantrell, C. A. and Stedman, D. H.: A possible technique for the measurement of atmospheric peroxy radicals, *Geophys. Res. Lett.*, 9, 846–849, 1982.
- 660 Cantrell, C. A., Stedman, D. H., and Wendel, G. J.: Measurement of atmospheric peroxy radicals by chemical amplification, *Anal. Chem.*, 56, 1496–1502, 1984
- Cantrell, C. A., Shetter, R. E., Calvert, J. G., Eisele, F. L., Williams, E., Baumann, K., Brune, W. H., Stevens, P. S., Mather J. H.: Peroxy radicals from photostationary state deviations and steady state calculations during the Tropospheric OH Photochemistry Experiment at Idaho Hill, Colorado, 1993, *J. Geophys. Res.*, 102(D5), 6369, <https://doi.org/10.1029/96JD01703>, 1997.
- 665 Cantrell, C. A., G. D. Edwards, S. Stephens, L. Mauldin, E. Kosciuch, M. Zondlo, and F. Eisele.: Peroxy radical observations using chemical ionisation mass spectrometry during TOPSE, *J. Geophys. Res.*, 108(D6), 8381, <https://doi.org/10.1029/2002JD002715>, 2003a.
- 670 Cantrell, C. A., Edwards, G. D., Stephens, S., Mauldin, R.L., Zondlo, M.A., Kosciuch, E., Eisele, F. L., Shetter, R. E., Lefer, B. L., Hall, S., Flocke, F., Weinheimer, A., Fried, A., Apel, E., Kondo, Y., Blake, D. R., Blake, N. J., Simpson, I. J., Bandy, A. R., Thornton, D. C., Heikes, B. G., Singh, H. B., Brune, W. H., Harder, H., Martinez, M., Jacob, D. J., Avery, M. A., Barrick, J. D., Sachse, G. W., Olson, J. R., Crawford, J. H., and Clarke, A. D.: Peroxy radical behaviour during the Transport and Chemical Evolution over the Pacific (TRACE-P) campaign as measured aboard the NASA -3B aircraft, *J. Geophys. Res.*, 108(D20), 8797, <https://doi.org/10.1029/2003JD003674>, 2003b.
- 675 Chen H., Winderlich, J., Gerbig, C., Hofer, A., Rella, C. W., Crosson, E. R., Van Pelt, A. D., Steinbach, J., Kolle, O., Beck, V., Daube, B. C., Gottlieb, E. W., Chow, V. Y., Santoni, G. W., and S. C. Wofsy, High-accuracy continuous airborne measurements of greenhouse gases (CO<sub>2</sub> and CH<sub>4</sub>) using the cavity ring-down spectroscopy (CRDS) technique, *Atmos. Mes. Tech.*, 3, 375-386, 2010.
- 680 Crawford, J., Davis, D., Olson, J., Chen, G., Liu, S., Gregory, G., Barrick, J., Sachse, G., Sandholm, S., Heikes, B., Singh, H., and Blake, D.: Assessment of upper tropospheric HO<sub>x</sub> sources over the tropical Pacific based on NASA GTE/PEM data: Net effect on HO<sub>x</sub> and other photochemical parameters, *J. Geophys. Res.*, 104, 16255–16273, <https://doi.org/10.1029/1999JD900106>, 1999.
- Fisher, R., Lowry, D., Wilkin, O., Sriskantharajah, S., and Nisbet, E. G.: High-precision, automated stable isotope analysis of atmospheric methane and carbon dioxide using continuous-flow isotope-ratio mass spectrometry, *Rapid communications in mass spectrometry: RCM*, 20 (2), 200–208. <https://doi.org/10.1002/rcm.2300>, 2006.
- 685 Fricke, C., Ehrlich, A., Jäkel, E., Bohn, B., Wirth, M., and Wendisch, M.: Influence of local surface albedo variability and ice crystal shape on passive remote sensing of thin cirrus, *Atmos. Chem. Phys.*, 14, 1943-1958, <https://doi.org/10.5194/acp-14-1943-2014>, 2014.
- 690 General, S., Pöhler, D., Sihler, H., Bobrowski, N., Frieß, U., Zielcke, J., Horbanski, M., Shepson, P. B., Stirm, B. H., Simpson, W. R., Weber, K., Fischer, C., and Platt, U.: The Heidelberg Airborne Imaging DOAS Instrument (HAIDI) – a novel Imaging DOAS device for 2-D and 3-D imaging of trace gases and aerosols, *Atmos. Meas. Tech.*, 7, 3459-3485, 2014, <https://doi.org/10.5194/amt-7-3459-2014>.

- George, M., Andrés-Hernández, M. D., Nenakhov, V., Liu, Y., and Burrows, J. P.: Airborne measurement of peroxy radicals using chemical amplification coupled with cavity ring-down spectroscopy: the PerCEAS instrument, *Atmos. Meas. Tech.* 13, 2577–2600, <https://doi.org/10.5194/amt-13-2577-2020>.
- George, M. *Phd thesis*, Airborne measurement and interpretation of peroxy radical concentrations with a focus on the oxidation mechanisms in the Asian free troposphere, PhD thesis, [University of Bremen 2022](#)
- 695
- Gerbig, C., Kley, D., Volz-Thomas, A., Kent, J., Dewey, K., and McKenna, D. S.: Fast response resonance fluorescence CO measurements aboard the C-130: Instrument characterisation and measurements made during North Atlantic Regional Experiment 1993, *J. Geophys. Res.*, 101, 29229–29238, 1996.
- Griffith, S. M., Hansen, R. F., Dusanter, S., Michoud, V., Gilman, J. B., Kuster, W. C., Veres, P. R., Graus, M., de Gouw, J. A., Roberts, J., Young, C., Washenfelder, R., Brown, S. S., Thalman, R., Waxman, E., Volkamer, R., Tsai, C., Stutz, J., Flynn, J. H., Grossberg, N., Lefer, B., Alvarez, S. L., Rappenglueck, B., Mielke, L. H., Osthoff, H. D., and Stevens, P. S.: Measurements of Hydroxyl and Hydroperoxy Radicals during CalNexLA: Model Comparisons and Radical Budgets, *J. Geophys. Res.-Atmos.*, 121, 4211–4232, <https://doi.org/10.1002/2015JD024358>, 2016.
- 700
- Horstjann, M., Andrés Hernández, M. D., Nenakhov, V., Chrobry, A., and Burrows, J. P.: Peroxy radical detection for airborne atmospheric measurements using absorption spectroscopy of NO<sub>2</sub>, *Atmos. Meas. Tech.* 7, 1245–1257, <https://doi.org/10.5194/amt-7-1245-2014>.
- 705
- Hüneke, T., Aderhold, O.-A., Bounin, J., Dorf, M., Gentry, E., Grossmann, K., Groß, J.-U., Hoor, P., Jöckel, P., Kenntner, M., Knapp, M., Knecht, M., Lörks, D., Ludmann, S., Matthes, S., Raecke, R., Reichert, M., Weimar, J., Werner, B., Zahn, A., Ziereis, H., and Pfeilsticker, K.: The novel HALO mini-DOAS instrument: inferring trace gas concentrations from airborne UV/visible limb spectroscopy under all skies using the scaling method, *Atmos. Meas. Tech.*, 10, 4209–4234, <https://doi.org/10.5194/amt-10-4209-2017>, 2017.
- 710
- Inomata, S., Tanimoto, H., Kameyama, S., Tsunogai, U., Irie, H., Kanaya, Y., and Wang, Z.: Technical Note: Determination of formaldehyde mixing ratios in air with PTR-MS: laboratory experiments and field measurements, *Atmos. Chem. Phys.*, 8, 273–284, <https://doi.org/10.5194/acp-8-273-2008>, 2008.
- 715
- Kanaya, Y., Fukuda, M., Akimoto, H., Takegawa, N., Komazaki, Y., Yokouchi, Y., Koike, M., and Kondo, Y.: Urban photochemistry in central Tokyo: 2. Rates and regimes of oxidant (O<sub>3</sub> + NO<sub>2</sub>) production, *J. Geophys. Res.*, 113, D06301, <https://doi.org/10.1029/2007JD008671>, 2008.
- Kanaya, Y., Hofzumahaus, A., Dorn, H.-P., Brauers, T., Fuchs, H., Holland, F., Rohrer, F., Bohn, B., Tillmann, R., Wegener, R., Wahner, A., Kajii, Y., Miyamoto, K., Nishida, S., Watanabe, K., Yoshino, A., Kubistin, D., Martinez, M., Rudolf, M., Harder, H., Berresheim, H., Elste, T., Plass-Dülmer, C., Stange, G., Kleffmann, J., Elshorbany, Y., and Schurath, U.: Comparisons of observed and modeled OH and HO<sub>2</sub> concentrations during the ambient measurement period of the HO<sub>x</sub>Comp field campaign, *Atmos. Chem. Phys.*, 12, 2567–2585, <https://doi.org/10.5194/acp-12-2567-2012>, 2012.
- 720

- 725 Kartal, D., Andrés-Hernández, M. D., Reichert, L., Schlager, H., and Burrows, J. P.: Technical Note: Characterisation of a DUALER instrument for the airborne measurement of peroxy radicals during AMMA 2006, *Atmos. Chem. Phys.*, 10, 3047–3062, <https://doi.org/10.5194/acp-10-3047-2010>, 2010.
- Kleinman, L., Y.-N. Lee, S. R. Springston, J. H. Lee, L. Nunnermacker, J. Weinstein-Lloyd, X. Zhou, and L. Newman, Peroxy radical concentration and ozone formation rate at a rural site in southeastern United States, *J. Geophys. Res.*, 100, 7263– 7273, 1995.
- 730 Kluge, F., Hüneke, T., Knecht, M., Lichtenstern, M., Rotermund, M., Schlager, H., Schreiner, B., and Pfeilsticker, K.: Profiling of formaldehyde, glyoxal, methylglyoxal, and CO over the Amazon: normalized excess mixing ratios and related emission factors in biomass burning plumes, *Atmos. Chem. Phys.*, 20, 12363–12389, <https://doi.org/10.5194/acp-20-12363-2020>, 2020.
- Lew, M. M., Rickly, P. S., Bottorff, B. P., Reidy, E., Sklaveniti, S., Léonardis, T., Locoge, N., Dusanter, S., Kundu, S., Wood, E., and Stevens, P. S.: OH and HO<sub>2</sub> radical chemistry in a midlatitude forest: measurements and model comparisons, *Atmos. Chem. Phys.*, 20, 9209–9230, <https://doi.org/10.5194/acp-20-9209-2020>, 2020.
- 735 Mallaun, C., Giez, A. and Baumann, R.: Calibration of 3-D wind measurements on a single engine research aircraft *Atmos. Meas. Tech.*, 8, 3177-3196, <https://doi.org/10.5194/amt-8-3177-2015>, 2015.
- Mao, J., Jacob, D. J., Evans, M. J., Olson, J. R., Ren, X., Brune, W. H., Clair, J. M. St., Crouse, J. D., Spencer, K. M., Beaver, M. R., Wennberg, P. O., Cubison, M. J., Jimenez, J. L., Fried, A., Weibring, P., Walega, J. G., Hall, S. R., Weinheimer, A. J., Cohen, R. C., Chen, G., Crawford, J. H., McNaughton, C., Clarke, A. D., Jaeglé, L., Fisher, J. A., Yantosca, R. M., Le Sager, P., and Carouge, C.: Chemistry of hydrogen oxide radicals (HO<sub>x</sub>) in the Arctic troposphere in spring, *Atmos. Chem. Phys.*, 10, 5823–5838, <https://doi.org/10.5194/acp-10-5823-2010>, 2010.
- 740 Parrish, D. D., Trainer, M., Williams, E. J., Fahey, D. W., Hobler, G., Eubank, C. S., Liu, S.C., Murphy, P. C. , Albritton, D. L. and Fehsenfeld, F. C.: Measurements of the NO<sub>x</sub>-O<sub>3</sub> photostationary state at Niwot Ridge, Colorado, *J. Geophys. Res.*, 91, No.D5, 5361 – 5370, 1986.
- 745 Ren, X., Harder, H., Martinez, M., Leshner, R. L., Olinger, A., Shirley, T., Adams, J., Simpas, J. B., and Brune, W. H.: HO<sub>x</sub> concentrations and OH reactivity observations in New York City during PMTACS-NY2001, *Atmos. Environ.*, 37, 3627–3637, 2003.
- 750 Ren, X., van Duin, D., Cazorla, M., Chen, S., Mao, J., Zhang, L., Brune, W. H., Flynn, J. H., Grossberg, N., Lefer, B. L., Rappenglück, B., Wong, K. W., Tsai, C., Stutz, J., Dibb, J. E., Thomas Jobson, B., Luke, W. T., and Kelley, P.: Atmospheric oxidation chemistry and ozone production: Results from SHARP 2009 in Houston, Texas, *J. Geophys. Res.*, 118, 5770–5780, <https://doi.org/10.1002/jgrd.50342>, 2013.
- Ren, Y., Baumann, R., Schlager, H.: An airborne perfluorocarbon tracer system and its first application for a Lagrangian experiment. *Atmos. Meas. Tech.*, 8, 69-80. <https://doi.org/10.5194/amt-8-69-2015>, 2015.



- 755 Ridley, B.A., Madronich, S., Chatfield, R. B., Walega, J. G., and Shetter, R. E.: Measurements and model simulations of the photostationary state during the Mauna Loa observatory photochemistry experiment: Implications for radical concentrations and ozone production and loss rates, *J. Geophys. Res.* **97**, 10375-10388 (1992).
- 760 Rotermund, M. K., Bense, V., Chipperfield, M. P., Engel, A., Groöß, J.-U., Hoor, P., Hüneke, T., Keber, T., Kluge, F., Schreiner, B., Schuck, T., Vogel, B., Zahn, A., and Pfeilsticker, K.: Organic and inorganic bromine measurements around the extratropical tropopause and lowermost stratosphere: Insights into the transport pathways and total bromine, *Atmos. Chem. Phys. Discuss.* [preprint], <https://doi.org/10.5194/acp-2021-202>, in review, 2021.
- Stutz, J., Werner, B., Spolaor, M., Scalone, L., Festa, J., Tsai, C., Cheung, R., Colosimo, S. F., Tricoli, U., Raecke, R., Hossaini, R., Chipperfield, M. P., Feng, W., Gao, R.-S., Hints, E. J., Elkins, J. W., Moore, F. L., Daube, B., Pittman, J., Wofsy, S., and Pfeilsticker, K.: A new Differential Optical Absorption Spectroscopy instrument to study atmospheric chemistry from a high-altitude unmanned aircraft, *Atmos. Meas. Tech.*, **10**, 1017 – 1042, <https://doi.org/10.5194/amt-10-1017-2017>, 2017.
- 765 Schulz, C., Schneider, J., Holanda, B. A., Appel, O., Costa, A., de Sá, S.S., Dreiling, V., Fütterer, D., Jurkat-Witschas, T., Klimach, T., Knöte, C., Krämer, M., Martin, S.T., Mertes, S., Pöhlker, M.L., Sauer, D., Voigt, C., Walser, A., Weinzierl, A.B., Ziereis, H., Zöger, M., Andreae, M.O., Artaxo, P., Machado, L.-A.T., Pöschl, U., Wendisch, M., and S. Borrmann, Aircraft-based observations of isoprene-epoxydiol-derived secondary organic aerosol (IEPOX-SOA) in the tropical upper troposphere over the Amazon region. *Atmos. Chem. Phys.*, **18**, 14979–15001, 2018, <https://doi.org/10.5194/acp-18-14979-2018>.
- 770 Schumann, U.: Measurement and model data comparisons for the HALO-FAAM formation flight during EMeRGe on 17 July 2017, [doi:10.5281/zenodo.4427965](https://doi.org/10.5281/zenodo.4427965), 2020.
- Speidel, M., Nau, R., Arnold, F., Schlager, H., A. Stohl, Sulfur dioxide measurements in the lower, middle and upper troposphere: Deployment of an aircraft-based chemical ionisation mass spectrometer with permanent in-flight calibration, *Atmospheric Environment*, **41**, 2427-2437, <https://doi.org/10.1016/j.atmosenv.2006.07.047>. 2007.
- 775 Tan, D., Faloon, I., Simpas, J. B., Brune, W., Olson, J., Crawford, J., Avery, M., Sachse, G., Vay, S., Sandholm, S., Guan, H.-W., Vaughn, T., Mastromarino, J., Heikes, B., Snow, J., Podolske, J., and Singh, H.: OH and HO<sub>2</sub> in the tropical Pacific: Results from PEMTropics B, *J. Geophys. Res.*, **106**, 32,667–32,681, 2001.
- 780 Tan, Z., Fuchs, H., Lu, K., Hofzumahaus, A., Bohn, B., Broch, S., Dong, H., Gomm, S., Häseler, R., He, L., Holland, F., Li, X., Liu, Y., Lu, S., Rohrer, F., Shao, M., Wang, B., Wang, M., Wu, Y., Zeng, L., Zhang, Y., Wahner, A., and Zhang, Y.: Radical chemistry at a rural site (Wangdu) in the North China Plain: observation and model calculations of OH, HO<sub>2</sub> and RO<sub>2</sub> radicals, *Atmos. Chem. Phys.*, **17**, 663–690, <https://doi.org/10.5194/acp-17-663-2017>, 2017.
- Tyndall, G. S.; Cox, R. A.; Granier, C.; Lesclaux, R.; Moortgat, G. K.; Pilling, M. J.; Ravishankara, A. R.; Wallington, T. J. Atmospheric chemistry of small organic peroxy radicals. *J. Geophys. Res.* **2001**, **106**, 12157-12182, <https://doi.org/10.1029/2000JD900746>.
- 785 Volz-Thomas, A., Xueref, I., and Schmitt, R.: Automatic gas chromatograph and calibration system for ambient measurements of PAN and PPN, *Environ. Sci. Poll. Res.*, **9**, 72-76, 2001.

Volz-Thomas, A., Pätz, H - W., Houben, N., Konrad, S., Mihelcic, D., Klüpfel, T., Perner, D.: Inorganic trace gases and peroxy radicals during BERLIOZ at Pabstthum: An investigation of the photostationary state of NO<sub>x</sub> and O<sub>3</sub>, *J. Geophys. Res.*, 108(D4), PHO 4-1, <https://doi.org/10.1029/2001JD001255>, 2003.

790 Wendisch, M., Pöschl, U., Andreae, M. O., Machado, L. A. T., Albrecht, R., Schlager, H., Rosenfeld, D., Martin, S. T., Abdelmonem, A. Afchine, A., Araùjo, A. C., Artaxo, P., Aufmhoff, H. Barbosa, H. M. J., Borrmann, S., Braga, R., Buchholz, B., Cecchini, M. A., Costa, A. Curtius, J., Dollner, M., Dorf, M., Dreiling, V., Ebert, V., Ehrlich, A., Ewald, F., Fisch, G., Fix, A., Frank, F., Fütterer, D., Heckl, C., Heidelberg, F., Hüneke, T., Jäkel, E., Järvinen, E., Jurkat, T., Kanter, S., Kästner, U., Kenntner, M., Kesselmeier, J., Klimach, T., Knecht, M., Kohl, R., Kölling, T., Krämer, M., Krüger, M., Krisna, T. C., Lavric, J. V., Longo, 795 K., Mahnke, C., Manzi, A. O., Mayer, B., Mertes, S., Minikin, A., Molleker, S., Münch, S., Nillius, B., Pfeilsticker, K., Pöhlker, C., Roiger, A., Rose, D., Rosenow, D., Sauer, D., Schnaiter, M., Schneider, J., Schulz, C., de Souza, R. A. F. Spanu, A., Stock, P., Vila, D., Voigt, C., Walser, A., Walter, D., Weigel, R., Weinzierl, B., Werner, F., Yamasoe, M. A., Ziereis, H., Zinner, T., and Zöger, M.: The ACRIDICON-CHUVA campaign: Studying tropical deep convective clouds and precipitation over Amazonia using the new German research aircraft HALO, *Bull. Amer. Meteorol. Soc.*, 97, 1885-1908, <https://doi.org/10.1175/BAMS-D-14-00255>, 2016. 800

Whalley, L. K., Slater, E. J., Woodward-Massey, R., Ye, C., Lee, J. D., Squires, F., Hopkins, J. R., Dunmore, R. E., Shaw, M., Hamilton, J. F., Lewis, A. C., Mehra, A., Worrall, S. D., Bacak, A., Bannan, T. J., Coe, H., Percival, C. J., Ouyang, B., Jones, R. L., Crilley, L. R., Kramer, L. J., Bloss, W. J., Vu, T., Kotthaus, S., Grimmond, S., Sun, Y., Xu, W., Yue, S., Ren, L., Acton, W. J. F., Hewitt, C. N., Wang, X., Fu, P., and Heard, D. E.: Evaluating the sensitivity of radical chemistry and ozone formation to ambient VOCs and NO<sub>x</sub> in Beijing, *Atmos. Chem. Phys.*, 21, 2125–2147, <https://doi.org/10.5194/acp-21-2125-2021>, 2021. 805

Wintel, J., Hösen, E., Koppmann, R., Krebsbach, M., Hofzumahaus, A., and Rohrer, F.: Stable carbon isotope ratios of toluene in the boundary layer and the lower free troposphere, *Atmos. Chem. Phys.*, 13, 11059-11071, <https://doi.org/10.5194/acp-13-11059-2013>, 2013.

Zahn, A., Weppner, J., Widmann, H., Schlote-Holubek, K., Burger, B., Kühner, T., Franke, H.: A fast and precise chemiluminescence ozone detector for eddy flux and airborne application, *Atmos. Meas. Tech.*, 5 (2), 363–375. <https://doi.org/10.5194/amt-5-363-2012>, 2012. 810

Zarzana, K. J., Min, K.-E., Washenfelder, R. A., Kaiser, J., Krawiec-Thayer, M., Peischl, J., Neuman, J. A., Nowak, J. B., Wagner, N. L., Dubè, W. P., St. Clair, J. M., Wolfe, G. M., Hanisco, T. F., Keutsch, F. N., Ryerson, T. B., and Brown, S. S.: Emissions of Glyoxal and Other Carbonyl Compounds from Agricultural Biomass Burning Plumes Sampled by Aircraft, *Environ. Sci. Technol.*, 51, 11761–11770, <https://doi.org/10.1021/acs.est.7b03517>, 2017. 815

Ziereis, H., Minikin, A., Schlager, H., Gayet, J.F., Auriol, F., Stock, P., Baehr, J., Petzold, A., Schumann, U., Weinheimer, A., Ridley, B., and Ström, J.: Uptake of reactive nitrogen on cirrus cloud particles during INCA, *Geophys. Res. Lett.*, 31(5), 2004.